

# Broad-band Spectral Modeling of Prompt Emission from Gamma-Ray Bursts Observed by the Transiting Exoplanet Survey Satellite

RAHUL JAYARAMAN,<sup>1</sup> MICHAEL FAUSNAUGH,<sup>2</sup> GEORGE R. RICKER,<sup>1</sup> AND ROLAND VANDERSPEK<sup>1</sup>

<sup>1</sup>*Department of Physics and Kavli Institute for Astrophysics and Space Research, Massachusetts Institute of Technology, 77 Massachusetts Ave, Cambridge, MA 02139, USA*

<sup>2</sup>*Department of Physics and Astronomy, Box 41051, Texas Tech University, Lubbock, TX 79409*

Submitted to ApJ

## ABSTRACT

Optical observations of gamma-ray bursts (GRBs) contemporaneous with their prompt high-energy emission are rare, but they can provide insights into the physical processes underlying these explosive events. The Transiting Exoplanet Survey Satellite’s (TESS) large field of view and continuous observation capabilities make it uniquely positioned to detect and characterize prompt optical flashes from GRBs. In this work, we fit phenomenological models to the gamma-ray through optical spectral energy distributions (SEDs) of 24 bursts with arcsecond-level localizations that fell within the TESS field of view between 2018 July and 2024 December. In four cases, the extrapolation of the high-energy SED agrees with the observed optical flux to within  $1\text{-}\sigma$ . In one case, there is a significant excess of optical flux relative to the extrapolation. In two cases, upper limits from TESS did not constrain the optical portion of the SED. In the remaining 17 cases, the optical flux is overpredicted by the extrapolation from high energies. This discrepancy could be explained by dust extinction in the host galaxy.

*Keywords:* Gamma-ray bursts, High-energy astrophysics, Gamma-ray astronomy

## 1. INTRODUCTION

Contemporaneous optical observations of gamma-ray bursts (GRBs) are rare when compared to the total number of GRBs that have been detected through observations at high energies. With the launch of numerous high-energy sky monitoring instruments, including the Burst Alert Telescope (BAT) on board the Neil Gehrels Swift Observatory (Gehrels et al. 2004), the Gamma-ray Burst Monitor (GBM) on board the Fermi Gamma-ray Space Telescope (Meegan et al. 2009), the Wide-field X-ray Telescope on board the Einstein Probe (Yuan et al. 2018, 2022), and the ECLAIRs telescope on board the Space Variable Objects Monitor (Wei et al. 2016), hundreds of GRBs are currently detected every year. However, it is difficult to obtain contemporaneous optical observations of GRBs. Telescopes either need to be pointed at the GRB at the time of trigger, or they

need to be able to rapidly slew to the localization region within a few seconds in order to observe the GRB during its high-energy emission. The first observation of optical emission from a GRB contemporaneous with its high-energy emission (Akerlof et al. 1999) was enabled by a telescope rapidly slewing to the localization of GRB 990123 from the Burst and Transient Source Experiment (BATSE) onboard the Compton Gamma-ray Observatory (Horack 1991). In this case, the earliest observation by the Robotic Optical Transient Search Experiment began 22 s after the BATSE trigger ( $t_0 + 22$  s).

Since the detection of GRB 990123, there have been only a few tens of detections of prompt optical emission, compared to the thousands of GRBs that have been observed. In four instances, there have been contemporaneous observations of the burst from before the time of trigger to well after the high-energy emission has concluded: Racusin et al. (2008) observed a “naked-eye” ( $V \sim 5.7$ ) optical flash from GRB 080319B, Vestrand et al. (2014) observed correlated emission between the optical light curve and the gamma-ray light curve above 100 MeV for GRB 130427A, Troja et al. (2017) observed

significant variable polarization during the prompt optical flash from GRB 160625B, and [Xin et al. \(2023\)](#) observed the prompt optical flash from GRB 201223A. Other detections of prompt flashes were enabled by ground-based telescopes rapidly slewing to cover the localization area calculated by high-energy sky survey instruments. Examples include the detections by [Vestrand et al. \(2005,  \$t\_0 + 115\$  s\)](#), [Klotz et al. \(2006,  \$t\_0 + 9\$  s\)](#), [Vestrand et al. \(2006,  \$t\_0 + 5.5\$  s\)](#), and [Oganesyan et al. \(2023,  \$t\_0 + 28\$  s\)](#). In addition to these detections, [Williams et al. \(2008\)](#) and [Klotz et al. \(2009\)](#) reported limits on optical flashes from GRBs using the LOTIS<sup>1</sup> and TAROT<sup>2</sup> networks, respectively.

Despite several observations of this phenomenon over the past three decades, the relationship between the prompt optical flash and the high-energy emission remains unclear. The prevailing theory for the mechanism underlying the prompt emission from a GRB is internal shocks in the jet that radiate via synchrotron emission ([Sari & Piran 1997](#)). [Kopač et al. \(2013\)](#) find evidence that the observed optical flashes in their sample of 36 GRBs are related to synchrotron radiation from internal shocks. However, the optical flux and the extrapolation from models for the high-energy emission often disagree by several orders of magnitude. In cases where the optical flux is suppressed relative to the extrapolation from the model for the high-energy emission, [Oganesyan et al. \(2017, 2018, 2019\)](#) suggest that an extra spectral break in soft X-rays could explain these observations. Such a break would physically correspond to the cooling break, in what they refer to as the “marginally fast-cooling regime” ([Kumar & McMahon 2008](#); [Beniamini & Piran 2013](#)). However, studies of GRB afterglows suggest that host galaxy extinction is an important effect and can also play a role in the observed properties of ultraviolet/optical prompt emission (e.g., [Perley et al. 2009](#); [Greiner et al. 2011](#)).

On the other hand, several GRBs have been observed with a significant flux excess when compared to the extrapolation of the high-energy model. For instance, [Xin et al. \(2023\)](#) found a deviation of over four orders of magnitude between the extrapolation of the power-law of the high-energy spectrum and the observed optical flux contemporaneous with GRB 201223A (see their Fig. 4); similarly, optical observations from [Oganesyan et al. \(2023\)](#) do not agree with an extrapolation of the power-law high-energy spectrum. A potential explanation for these observations is the presence of a reverse

shock in the GRB; this would be as energetic as the forward shock but radiate at optical wavelengths ([Mészáros & Rees 1999](#); [Sari & Piran 1999](#)). Reverse shocks also peak on relatively short timescales when compared to the peak of the forward shock light curve (referred to as the “afterglow”). Another explanation for these observations could be the presence of extra emission from the GRB photosphere ([Guiriec et al. 2015a,b, 2016a,b](#)); these models suggest that there exists an extra power-law component that evolves early on during the burst.

In this work, we present spectral modeling of GRBs with prompt optical observations from the Transiting Exoplanet Survey Satellite (TESS; [Ricker et al. 2015](#)). TESS’s continuous observing capabilities and large field of view enable the observation of prompt optical flashes from several GRBs per year. Our sample consists of 24 GRBs with arcsecond-level localizations from the X-ray Telescope (XRT) on board the Neil Gehrels Swift Observatory that were in the TESS field of view at the time of trigger. This sample, discussed in [Jayaraman et al. \(2024, hereafter J24\)](#), spans the first 6.5 years of the TESS mission (2018 July to 2024 December).

We organize this paper as follows: Section 2 provides information about the high-energy and optical observations. Section 3 presents our fits to the data and compares the extrapolation from high energies with the optical flux (or corresponding limits) from TESS. Finally, Section 4 discusses why a prompt optical flash might not be detected from all GRBs, and Section 5 summarizes our conclusions.

## 2. SAMPLE SELECTION, OBSERVATIONS, AND DATA PROCESSING

Our sample is based on the sample from J24, which consists of 22 bursts that had X-ray-detected afterglows from Swift-XRT. In addition to these bursts, we add two bursts (241030A and 241030B) that had optical counterparts in TESS—reported in GCNs 38134 ([Jayaraman et al. 2024](#)) and 38158 ([Jayaraman et al. 2024](#)), respectively. We also analyzed GRB 231106A, for which a candidate optical counterpart was identified in TESS ([Jayaraman et al. 2023b](#), GCN 35047). Information about the bursts in our sample, including their durations ( $T_{90}$ ), data availability, and limits on (or magnitudes of) the prompt optical flash, are given in Table 1. Information about the three additional bursts highlighted above is given in Table 2.

<sup>1</sup> Livermore Optical Transient Imaging System

<sup>2</sup> Télescopes à Action Rapide pour les Objets Transitoires

We used data from both Fermi and Swift to analyze the prompt gamma-ray spectral energy distribution (SED). We report time intervals that capture virtually

**Table 1.** Data availability for the prompt emission phase of each burst in our sample. We note that only GRB 241030A has a contemporaneous Swift-XRT observation of the prompt emission, and that Fermi-LAT data was available for GRBs 200412B (Longo et al. 2020) and 241030A (Pillera et al. 2024). We also list the  $T_{90}$  for each burst as catalogued by Fermi and Swift, the TESS magnitudes (or  $3\text{-}\sigma$  upper limits for bursts with no detections in TESS), and the value of  $F_\nu$  in Jy. Estimates for the prompt TESS magnitude of the optically-detected bursts are reproduced from the last column of Table 4 in Jayaraman et al. (2024) and have been corrected for the effects of cosmic-ray mitigation (see Appendix A in J24). However, we display the uncorrected measurements for GRBs 231106A and 241030B, and show the CRM-corrected measurements in Table 3.

Identifier	$T_{90}$ (s)	Swift- BAT	Fermi- GBM	Estimated Prompt $T_{\text{mag}}$	Prompt Flux (mJy)
GRB 180727A ‡	$1.1 \pm 0.2$	✓	✓	$> 18.74$	$< 0.08$
GRB 180924A ‡	$95.1 \pm 10.9$	✓	✗	$> 19.01$	$< 0.06$
GRB 181022A ‡	$6.74 \pm 2.30$	✓	✗	$> 18.98$	$< 0.07$
GRB 190422A ‡	$213.25 \pm 10.75$	✓	✓	$> 17.98$	$< 0.17$
GRB 190630C ‡	$38.4 \pm 9.3$	✓	✗	$> 17.88$	$< 0.18$
GRB 191016A	$219.70 \pm 183.35$	✓	✗	$> 18.76$	$< 0.08$
GRB 200303A ‡	$94.2 \pm 6.4$	✓	✓	$> 19.08$	$< 0.06$
GRB 200324A ‡	—	✓	✗	$> 18.87$	$< 0.07$
GRB 200412B*	$6.08 \pm 0.29$	✗	✓	5.7–11.5	$6810 \pm 6740$
GRB 200901A	$20.37 \pm 7.55$	✓	✓	13.8–15.6	$4.64 \pm 3.15$
GRB 210204A*	$206.85 \pm 2.29$	✗	✓	14.6–16.5	$2.19 \pm 1.54$
GRB 210419A ‡✗	$64.43 \pm 11.69$	✓	✗	$> 17.5^a$	$< 0.25$
GRB 210504A	$135.06 \pm 9.57$	✓	✗	$> 18.24$	$< 0.13$
GRB 210730A ‡	$3.86 \pm 0.66$	✓	✓	$> 17.66$	$< 0.22$
GRB 220319A ‡	$6.44 \pm 1.54$	✓	✗	$> 18.19$	$< 0.14$
GRB 220623A	$57.11 \pm 8.53$	✓	✗	13.8–15.6	$4.64 \pm 3.15$
GRB 220708A ‡	$4.4 \pm 1.0$	✓	✗	$> 17.99$	$< 0.16$
GRB 221120A ‡	$0.79 \pm 0.16$	✓	✓	$> 17.61$	$< 0.23$
GRB 230116D	$41.00 \pm 11.18$	✓	✓	$> 17.5$	$< 0.25$
GRB 230307A	$34.56 \pm 0.57$	✗	✓	12.6–13.4	$17.42 \pm 6.14$
GRB 230903A	$2.54 \pm 0.27$	✓	✓	12.5–16.8	$13.16 \pm 12.69$
GRB 231106A*	$23.552 \pm 1.049^b$	✗	✓	12.0–12.6	$32.24 \pm 8.69$
GRB 241030A	$165.63 \pm 1.280^b$	✓	✓	$> 17.5^c$	$< 0.25$
GRB 241030B	$6.8484 \pm 0.668^b$	✓	✓	12.64–16.4	$11.708 \pm 10.997$

NOTE—(a) This is an upper limit based on subtracting the variability from a nearby star that contaminated the photometric aperture, which represents a source of systematic error.

(b) Fermi-GBM Burst Catalog (von Kienlin et al. 2014; Gruber et al. 2014; Narayana Bhat et al. 2016; von Kienlin et al. 2020).

(c) GCN 38134 (Jayaraman et al. 2024).

\*: The prompt emission estimate is derived from an FFI cadence that likely included multiple emission components—including prompt emission from internal shocks, reverse shock emission, and the early afterglow.

‡: No optical emission (either prompt or afterglow) was detected in TESS.

all of the observed fluence by finding the interval during which 99.5% of the gamma-ray fluence was emitted (which we refer to as  $T_{99.5}$ ). This interval is calculated based on the 0.25% and 99.75% percentiles of the cumulative flux distribution. Although  $T_{99.5}$  suffers from a larger statistical uncertainty than  $T_{90}$  due to difficulty in pinpointing these values, most of the GRBs in our sample tend to be bright, making any such effect small.  $T_{99.5}$  intervals are provided for each burst in Tables 4–6, after subtracting a constant background from the light curves. For bursts detected by both Fermi-GBM and

Swift-BAT, we jointly fit both sets of data to the same model. We also added data from the Large Area Telescope onboard Fermi (Fermi-LAT; Atwood et al. 2009), as well as Swift-XRT data into our analysis when available. Further information about the models and methods used to fit the high-energy SEDs of these GRBs is given in Section 3.

## 2.1. Swift-BAT

We first downloaded the event data, quality map, and the auxiliary ray tracing file for the Swift-BAT-

**Table 2.** As Table 1 from Jayaraman et al. (2024), but for bursts detected between 2023 November–2024 December. These bursts have contemporaneous observations from TESS and, in the cases of 241030A and 241030B, localizations from Swift-XRT. Extinctions  $E_{B-V}$  are obtained from Schlafly & Finkbeiner (2011) via the NASA Extragalactic Database, and the correction factors in the last column were calculated using the coefficients from Cardelli et al. (1989).

Identifier	Coordinates (J2000)						Trigger		3- $\sigma$ Limit ( $T_{\text{mag}}$ )	$E_{B-V}$ (mag)	Extinction Correction
	Right Ascension			Declination			BTJD	Sector			
GRB 231106A	07h	33m	47.57s	29d	13m	28.2s <sup>a</sup>	3255.26234	71	17.5	0.052	0.909
GRB 241030A	22h	52m	33.35s	80d	26m	59.1s <sup>b</sup>	3613.74442	85	17.46 <sup>c</sup>	0.118	0.804
GRB 241030B	03h	23m	10.19s	34d	26m	49.3s <sup>d</sup>	3614.27981	85	17.51 <sup>e</sup>	0.18	0.717

NOTE—(a) GCN 35047 (Jayaraman et al. 2023b). (b) GCN 37962 (Beardmore et al. 2024). (c) GCN 38134 (Jayaraman et al. 2024) (d) GCN 37992 (Evans et al. 2024). (e) GCN 38158 (Jayaraman et al. 2024)

detected bursts from the Swift Gamma-Ray Burst Catalog (Lien et al. 2016).<sup>3</sup> Then, we generated mask-weighted light curves using `batbinevt` and subtracted a constant background (calculated from a time interval prior to the burst), after which we calculated  $T_{99.5}$ . We used `batbinevt` again to create a spectrum of the burst during the  $T_{99.5}$  portion; this spectrum was corrected for ray tracing during potential spacecraft slews (using the `batupdatephakw` command) and systematics (using the `batphasyserr` command with CALDB). More specifically, `batphasyserr` adds the BAT systematic error vector, which contains the fractional systematic error in all the BAT channels, to any generated spectrum file. Finally, we created a response matrix using `batdrngen`. The software for Swift-BAT’s coded-mask aperture generate background-subtracted spectra and light curves, without the need for a separate background spectrum.

## 2.2. Swift-XRT

For two bursts—GRBs 200412B and 241030A—we used Swift-XRT data as part of our modeling for the flare and the prompt emission, respectively. No other bursts had Swift-XRT data from the prompt phase of the emission that overlapped with the TESS observation. The Swift-XRT spectra were obtained from the Swift-XRT GRB Catalogue (Evans et al. 2009)<sup>4</sup>. For an input time range, the catalog website generates source and background spectra, response matrix files (`rmf`), and ancillary response files (`arf`). We used data between 0.5–10 keV for the prompt emission in GRB 241030A and that between 2–6 keV for the flare in GRB 200412B.

## 2.3. Fermi-GBM

For all the bursts that were detected by Fermi-GBM, we downloaded the time-tagged event (TTE) data from the online Fermi GBM catalog (von Kienlin et al. 2014; Gruber et al. 2014; Narayana Bhat et al. 2016; von Kienlin et al. 2020) hosted at HEASARC<sup>5</sup>, along with the response files, for the two NaI detectors that triggered on the burst, and the corresponding BGO detector (b0 for NaI detectors n0–n5, and b1 for NaI detectors n6–n11). There were no bursts for which the two NaI detectors corresponded to different BGO detectors. For the four bursts without corresponding Swift-BAT detections, we made light curves from the NaI detector with the highest counts, and used that to calculate the  $T_{99.5}$  interval from which we extracted the spectrum. We also selected a 20 s interval from before the burst emission to estimate the background spectrum. The  $T_{99.5}$  intervals are shown with the fit parameters in Tables 4–6.

We used the Fermi-GBM tools (Fermi Science Support Development Team 2019) to generate PHA2 files for each detector—3 spectra per burst. This format simultaneously stores information about both the background and source spectra. While many bursts exhibit multiple emission episodes, the TESS data typically yield only one point across the entire burst, so we perform a time-integrated analysis for most of the bursts, rather than analyzing each episode of emission. Note that for all bursts in our sample for which a prompt optical flash is detected, such emission (i.e., the entirety of  $T_{99.5}$ ) lies wholly within the exposure duration of a single TESS full-frame image (FFI). We then used the `gtbin` tool on the TTE files to generate spectra and background estimates for each burst. We only used the range of 10–500 keV for the NaI detectors, and 400–10 000 keV for the BGO detectors. We masked out the region between

<sup>3</sup> <https://swift.gsfc.nasa.gov/results/batgrbcatalog/>

<sup>4</sup> [https://www.swift.ac.uk/xrt\\_products/](https://www.swift.ac.uk/xrt_products/)

<sup>5</sup> <https://heasarc.gsfc.nasa.gov/W3Browse/fermi/fermigbrst.html>



30–50 keV (the iodine *K*-edge) when fitting, due to the anomalous NaI detector response there.

#### 2.4. *Fermi-LAT*

For each burst, we searched the Fermi-LAT GRB catalog (FERMILGRB<sup>6</sup> on HEASARC) to check whether high-energy photons were detected from the burst. The online catalog is complete up to 2022 May 27, so we manually checked the General Circulars Network (GCN) for GRBs discovered after this date to determine whether any Fermi-LAT detections were reported for these bursts. Only two bursts (GRB 200412B, and GRB 241030A—Pillera et al. 2024) had detections by Fermi-LAT at the time of trigger. All the other bursts’ localizations were over 60° from the Fermi-LAT bore-sight at the time of trigger.

For our analysis, we downloaded the “extended” data from the LAT Data Query portal<sup>7</sup>. First, we filtered out emission from the Earth’s limb by imposing a cut on events above a zenith angle of 100° using `gtselect`. We then created a count map and a light curve using `gtbin`, after which we constructed a three-component model for the emission using `modeler`. This model comprised a point source at the GRB location, an isotropic component (for the extragalactic diffuse and residual background), and a Galactic diffuse emission component (defined in the `gll_iem_v07` file).<sup>8</sup> Finally, we generated an exposure map with `gtexpmap`, and generated the PHA and response files using `gtbin` and `gtrspgen`.

#### 2.5. *Optical Data from TESS*

To obtain a value for the optical flux, we utilized the procedure detailed in J24: We first used images from the TESS Image CALibrator (TICA) pipeline (Fausnaugh et al. 2020) as input to the difference imaging code described in Fausnaugh et al. (2021, 2023a), and then performed forced photometry at the Swift-XRT location.

The FFI cadence at the time of prompt emission was corrected for TESS’s cosmic ray mitigation (CRM) strategy, as described in Appendix A of J24. To summarize, the TESS cosmic ray mitigation procedure removes the brightest and faintest 2 s sub-exposures (per pixel) in a time window of 20 seconds. As a result, the CRM can also clip flux from flares that vary on the order of 10 seconds or less. Accounting for the effects of CRM results in typical corrections of roughly 20–25%

to the observed optical flux. Our correction technique assumes that the shape of the optical light curve is the same as the shape of the high energy light curve, up to a constant scaling factor (see, e.g., Vestrand et al. 2005; Racusin et al. 2008; Vestrand et al. 2014).<sup>9</sup> We calculated an estimated range for the magnitude (reported in Table 1) of the prompt optical flash based on the uncertainty in the duration of the optical emission. We assume that the minimum duration is the duration of the high energy emission itself (using  $T_{90}$  as a lower limit for this value), while the maximum duration is the interval from the start of the prompt high-energy emission to the end of the concurrent FFI exposure. Our conservative estimates for the lower and upper limits on the emission duration are required due to TESS’s (comparatively) long exposure times. Further details about the CRM strategy and flux calibration with TESS can be found in TESS’s Instrument Handbook<sup>10</sup>, as well as Appendix A of J24. In some cases, the CRM correction was negligible. Table 3 shows the CRM corrections for the two new bursts in our sample that exhibited evidence for a prompt optical flash, with columns mirroring those from Table 4 in J24.

We use TESS Vega-system magnitudes<sup>11</sup> throughout this paper (unless otherwise indicated), with  $T_{\text{mag}} = 0$  corresponding to 2583 Jy (J24). Throughout our analysis, we report light curves and flux measurements in  $\nu F_{\nu}$  units ( $\text{erg cm}^{-2} \text{s}^{-1}$ );  $\nu$  is the frequency corresponding to the TESS passband pivot wavelength of 784 nm ( $\nu_{\text{pivot}} = 3.824 \times 10^{14} \text{ Hz}$ ). All optical fluxes shown in the Figures have been corrected for Galactic extinction using the factors in Table 1 from J24 and the rightmost column from Table 2; these values were calculated using the procedure detailed in Section 2.2 of J24.

### 3. ANALYSIS AND RESULTS

To fit the high-energy spectra, we used the XSPEC package (Arnaud 1996). For bursts only detected by Swift-BAT, which is most sensitive between 15 and 150 keV,<sup>12</sup> we fit a pegged power-law (the XSPEC model `pegpwrlw`) to the prompt emission, with pegs at 15 and 150 keV. This model is similar to the `pow` model from XSPEC, but fits the power law only within the specified

<sup>6</sup> Information about this catalog can be found in Ajello et al. (2019)

<sup>7</sup> <https://fermi.gsfc.nasa.gov/cgi-bin/ssc/LAT/LATDataQuery.cgi>

<sup>8</sup> Available at <https://fermi.gsfc.nasa.gov/ssc/data/access/lat/BackgroundModels.html>.

<sup>9</sup> There are also several GRBs for which such a correlation is not observed, however.

<sup>10</sup> [https://archive.stsci.edu/missions/tess/doc/TESS\\_Instrument\\_Handbook\\_v0.1.pdf](https://archive.stsci.edu/missions/tess/doc/TESS_Instrument_Handbook_v0.1.pdf)

<sup>11</sup> The TESS passband response is available at <https://heasarc.gsfc.nasa.gov/docs/tess/data/tess-response-function-v2.0.csv>.

<sup>12</sup> [https://swift.gsfc.nasa.gov/analysis/bat\\_digest.html](https://swift.gsfc.nasa.gov/analysis/bat_digest.html)

**Table 3.** As Table 4 in J24, with the fluxes, fluences, and CRM corrections for the two bursts in our sample (GRBs 231106A and 241030B) discovered since mid-2023 that exhibit evidence for prompt optical emission. The second column is the observed fluence in the prompt FFI counts; the third is the estimated magnitude of the GRB at the time of trigger, calculated across the entire FFI exposure time. The fourth column is an estimate of the fluence from the afterglow in the FFI cadence spanning the time of trigger, based on an extrapolation of the best-fit power-law to the time of trigger. The fifth column gives the corrected flux, by subtracting column 4 from column 2 and then correcting for the TESS CRM algorithm. The sixth column provides an estimated range for the magnitude of the prompt emission; this value is calculated using the burst’s  $T_{90}$  as a lower limit for the emission duration, and the interval between the trigger time and the end of the contemporaneous FFI as the upper limit.

Identifier	Observed Fluence in Prompt FFI (counts)	Peak Observed Magnitude (TESS band)	Afterglow Contribu- tion in Prompt FFI (counts)	Corrected Prompt Flux (counts)	Corrected $T_{\text{mag}}$ of Prompt Emission
231106A	$6.89 \pm 0.20 \times 10^4$	$13.84 \pm 0.05$	$4.71 \pm 0.20 \times 10^4$	$2.84 \pm 0.30 \times 10^4$	12.7–14.4
241030B	$6.58 \pm 0.47 \times 10^3$	$16.40 \pm 0.08$	–	$1.36 \pm 0.2 \times 10^4$	12.16–15.25

range. This power-law had the form

$$A(E) = KE^{-\alpha}, \quad (1)$$

where  $K$  is the normalization over the selected energy range (here 15–150 keV), and  $\alpha$  is the power-law index. Note that the power-law index in this expression is used to fit the decay in photon flux ( $\text{ph cm}^{-2} \text{s}^{-1} \text{keV}^{-1}$ ) as a function of energy in keV. We report the photon index for fits in these units, but we show the high-energy spectra in energy units ( $\text{erg s}^{-1} \text{cm}^{-2}$ ) in Figures 1–3 and 4–6. The physical flux was determined using the `eeuf` command, which calculates  $\lambda^2 f(\lambda)$  and  $E^2 f(E)$ .

For bursts with Fermi-GBM data, we fit models that allow for a high-energy break—either a cutoff power-law model or the Band function (Band et al. 1993). The cutoff power-law (the `XSPEC` model `cutoffpl`) differs from a standard power-law due to the addition of an exponential high-energy power-law cutoff at an energy  $E_c$ :

$$A(E) = KE^{-\alpha} e^{-E/E_c}. \quad (2)$$

The Band function (`grbm` in `XSPEC`) is a phenomenological model with four parameters—a low-energy power-law index  $\alpha$ , a high-energy power-law index  $\beta$ , a peak/turnover energy  $E_p$ , and a normalization  $K$ :

$$\begin{cases} K \left( \frac{E}{100 \text{ keV}} \right)^{\alpha} \exp \left( -\frac{E}{E_0} \right), & (\alpha - \beta)E_p \geq E \\ K \left[ \frac{(\alpha - \beta)E_0}{100 \text{ keV}} \right]^{\alpha - \beta} \exp(\beta - \alpha) \left( \frac{E}{100 \text{ keV}} \right)^{\beta}, & (\alpha - \beta)E_p \leq E. \end{cases} \quad (3)$$

For most bursts,  $E_p$  and  $E_c$  are greater than 150 keV. Additionally, the convention for power-law indices differs between the power-law models and the Band function. For consistency, we report everything as the actual power-law index for the data, so the power-law indices ( $\alpha$ ) from the cutoff power-law and the pegged power-laws are reported as negative values, unlike in the default output provided by `XSPEC`.

For bursts with both Swift-BAT and Fermi-GBM data, we multiplied the Swift-BAT data by a constant

factor (using the `XSPEC` model `const`) to account for any calibration offsets between the two detectors (which can differ by up to 15%). We added another multiplicative calibration factor when analyzing Swift-XRT data in conjunction with other data sets. In addition, when fitting the Swift-XRT data, we added an absorption model for energies below 10 keV. We used two `tbabs` components—one to account for Galactic absorption, and another for absorption in the GRB host galaxy or intergalactic medium. To calculate the Galactic hydrogen column density, we used the `nh` utility in `XSPEC`, which uses maps from HI4PI Collaboration et al. (2016) and abundances from Wilms et al. (2000). For GRB 241030A, which has a known redshift, we use the `ztbabs` model, with  $z = 1.411$  (Zheng et al. 2024; Li et al. 2024).

Prior to fitting to the models, we binned Fermi-GBM spectra using the `ftgrouppha` tool to ensure that each bin had a minimum of 20 counts prior to fitting, using the optimal strategy detailed in Kaastra & Bleeker (2016). Swift-BAT data already have Gaussian statistics when using the mask-weighting technique.<sup>13</sup> We minimized  $\chi^2$  (`chi`) as our likelihood function for most cases. However, for Fermi-LAT data—which have a Poisson likelihood—we used `Cstat` (Cash 1979) instead. Similarly, due to the low number of counts in the Swift-XRT data for the flare in GRB 200412B, we also used `Cstat`. To calculate 90% confidence intervals for each best-fit parameter we used the `err` command in `XSPEC`, which varies the parameters until the calculated fit statistic is within the given tolerance value of the previously-calculated best-fit statistic. We rebinned data for aesthetic purposes in all the Figures using `setplot rebin`, with a significance of  $5\sigma$ .

Best-fit parameters for all the GRBs are reported in Tables 4–6. The physical interpretations of our modeling are further discussed in Section 4. For GRB 220623A,

<sup>13</sup> <https://swift.gsfc.nasa.gov/analysis/swiftbat.pdf>

which had a clear high-energy precursor in the Swift-BAT data, we fit the spectra of the precursor and the main burst separately to check for changing spectral properties. We did not find optical precursors using TESS down to the limiting magnitudes given in Table 1. These limits are consistent with previous results: Krimm et al. (1996) report no precursors down to 6th magnitude, Greiner et al. (1995) report limits of 12–14th magnitude for photographic plates covering the entirety of the BATSE localization region, and Blake & Bloom (2004) report 17–20th magnitude limits for precursors using observations from a 1-m class telescope.

Sections 3.1–3.3 discuss the spectral fits for GRBs that have a clearly-detected (or inferred) prompt optical emission component in the TESS data. This class of bursts can be divided into three classes: Those where the optical flux exceeds the extrapolation from high energies (Section 3.1), those where the optical flux is consistent with the extrapolation (Section 3.2), and those where the optical flux is overpredicted by the extrapolation (Section 3.3). Bursts without a prompt optical detection in TESS are discussed in Section 3.4. Tables 4 and 5 show the best-fit parameters to a Band and (cutoff) power-law functions, respectively, for the high-energy emission from bursts that had a prompt optical detection in TESS. Table 6 shows the same information for bursts with upper limits on the optical flux from TESS, rather than detections.

Details on individual bursts are given in Appendix A.

### 3.1. GRBs with optical flux detections above the extrapolation

There was one burst where the optical flux was over an order of magnitude above the extrapolation from high energies for the prompt main burst emission—GRB 200412B (left panel of Figure 1). During these observations, the TESS observational cadence was 30 min—a single exposure could encompass both a prompt flash; reverse shock emission, which occurs on timescales of tens of minutes (e.g., Kobayashi & Zhang 2003); and early afterglow emission. We subtracted the estimated afterglow flux in this cadence prior to calculating the flux. A reverse shock would cause the measured flux to be much higher than expected for a prompt flash alone. However, we cannot disentangle these two contributions with TESS data alone. Our estimate for the flux, as a result, has a large uncertainty (see J24 and Figure 1). This uncertainty does not encompass the extrapolation from high energies, suggesting that most of the observed optical flux is plausibly reverse shock emission. If we assume that all the emission arises from a prompt optical flash instead, integrating the extrapolated spectrum

across the TESS bandpass and assuming a duration of optical emission comparable to  $T_{90}$  yields a TESS magnitude  $T \sim 7.5$ . Other explanations for short-timescale, early emission components in GRBs include an excess of decaying neutrons in the ejecta (Fan et al. 2009) or emission from late-time “residual” shocks occurring in optically thin ejecta far from the progenitor ( $R \gtrsim 10^{15}$  cm; Li & Waxman 2008). However, a reverse shock remains the most robust prediction.

*Flare in 200412B*—GRB 200412B exhibited a flare at roughly  $2 \times 10^4$  s post-trigger. Given that there exists contemporaneous Swift-XRT data alongside the optical observations from TESS, we compared the extrapolation of the high-energy time-averaged spectrum of the flare to the TESS observations. We fit the Swift-XRT data as described in Section 2.2, masking data outside the 2–6 keV band in order to ensure that there was at least 1 count per bin. For the goodness-of-fit metric, we used the C-statistic (Cash 1979). We found a power-law index of  $-1.27^{+1.06}_{-1.05}$  for the high-energy emission. The optical flux, after subtracting the estimated afterglow flux (from the model in J24), is underpredicted by the extrapolation from high energies (Fig. 1) by over an order of magnitude. This optical flare has  $\Delta t/t \sim 0.1$ ; this parameter measures the duration of the flare  $\Delta t$  over the time since the trigger  $t_0$ . We also calculate  $\Delta F/F = 1.45$ , which calculates the flux excess of the flare peak relative to the power-law-decaying afterglow.

Using these calculated parameters, we can eliminate the possibilities for a flare using all the models that were explored in Kumar et al. (2022). Following their line of arguments (used for GRB 210204A), *the most likely explanation for this flare, based upon its duration and flux excess (relative to the afterglow), is late-time central engine activity*. This conclusion is borne out by the fact that our values for  $\Delta t/t$  and  $\Delta F/F$  are consistent with the overall distribution of flare parameters presented in Figure 11 of Kumar et al. (2022), suggesting that the flare in GRB 200412B has similar properties and/or a common origin to those presented in Swenson et al. (2013). However, our ability to draw conclusions from the TESS data and the Swift-XRT data is rather limited, given that we only have two photometric X-ray measurements at late times that coincide with the flare seen in the TESS light curve (Fig. 3 in J24).

### 3.2. GRBs with optical fluxes consistent with the extrapolations

GRBs 220623A, 230903A, 231106A, and 241030B exhibit prompt optical emission that is consistent with the high-energy extrapolation at  $1\text{-}\sigma$ . SEDs of the prompt emission are shown in Figure 2. For GRB 220623A, the

**Table 4.** Best-fit parameters for a Band function fit (Band et al. 1993). The second column lists the time interval over which the burst was fit ( $T_{99.5}$ ). The next three columns are the Band function parameters:  $\alpha$ , the low-energy spectral slope;  $\beta$ , the high-energy spectral slope; and  $E_p$ , the turnover (“peak”) energy. The final column shows the fit statistic for each burst, as calculated by XSPEC. Uncertainties are reported for each parameter as 90% confidence intervals.

Identifier	Fit Interval	$\alpha$ (Photon Index)	$\beta$	$E_p$ (keV)	Fit Statistic/dof <sup>a</sup>
GRB 200412B	$[t_0 - 2.67, t_0 + 22.3]$	$-0.98 \pm 0.08$	$-2.73^{+0.08}_{-0.09}$	$351.0^{+54.0}_{-46.2}$	114.86/100
GRB 210204A	$[t_0 + 149.4, t_0 + 277.0]$	$-1.31^{+0.50}_{-0.31}$	$-2.64^{+0.48}_{-0.68}$	$228^{+284}_{-121}$	129.29/109
GRB 230307A	$[t_0 - 1.62, t_0 + 100.48]$	$-0.95 \pm 0.01$	$-6.35^{+0.67}_{-3.39}$	$865^{+11}_{-15}$	678.26/206
GRB 241030A <sup>b</sup>	$[t_0 - 0.08, t_0 + 221.12]$	$-1.04 \pm 0.04$	$-2.51 \pm 0.06$	$101 \pm 7$	1270/1081

NOTE—(a) In most cases, this will be  $\chi^2$  per degree of freedom (dof); however, for the two bursts with Fermi-LAT data (200412B and 241030A), we report the combination of  $\chi^2$  for Fermi-GBM data and Cstat for the Fermi-LAT data. (b) The normalization parameter (to the Fermi-GBM spectrum) for Swift-BAT was  $0.89 \pm 0.02$ ; for Swift-XRT, it was  $2.8^{+0.21}_{-0.19}$ . Our best-fit estimate for the intrinsic hydrogen absorption was  $N_H = 7.47 \times 10^{21} \text{ cm}^{-2}$ .

**Table 5.** As Table 4, but for the (cutoff) power-law fits to GRB spectra. The photon power-law index is given by  $\alpha$ . Some of these bursts have data from both Fermi-GBM and Swift-BAT, so we introduced a constant factor to account for calibration differences between the two detectors’ responses; these values are enumerated in the last column. GRB 220623A, which had only Swift-BAT data, was fit to a pegged power-law between 15 and 150 keV. We also fit the precursor to this burst using the same model.

Identifier	Fit Interval	$\alpha$	$E_c$ (keV)	Fit Statistic/dof	Cross-Detector Normalization
GRB 200901A	$[t_0 - 5.02, t_0 + 20.28]$	$-1.42^{+0.25}_{-0.21}$	$313^{+173}_{-150}$	124.89/175	$0.91^{+1.16}_{-0.46}$
GRB 210204A	$[t_0 - 20.61, t_0 + 373.69]$	$-1.30^{+0.51}_{-0.81}$	$250^{+1600}_{-160}$	144.56/125	—
GRB 210204A	$[t_0 + 149.4, t_0 + 277.0]$	$-1.40^{+0.24}_{-0.29}$	$290^{+260}_{-110}$	129.69/110	—
GRB 220623A	$[t_0 - 4.28, t_0 - 2.88]$	$-0.70 \pm 0.14$	—	44.98/58	—
GRB 220623A	$[t_0 - 3.98, t_0 + 64.82]$	$-1.31 \pm 0.07$	—	54.04/58	—
GRB 230903A	$[t_0 - 0.92, t_0 + 4.4]$	$-1.01^{+0.76}_{-0.06}$	$88^{+388}_{-5}$	136.97/156	$0.83^{+0.36}_{-0.17}$
GRB 231106A <sup>†</sup>	$[t_0 - 18.34, t_0 + 40.76]$	$-0.88^{+0.33}_{-0.41}$	$81.3^{+66.1}_{-31.0}$	148.75/126	—
GRB 241030B	$[t_0 - 1.44, t_0 + 8.96]$	$-0.85^{+0.20}_{-0.22}$	$128.4^{+64.1}_{-36.3}$	178.86/208	$0.73 \pm 0.09$

best-fit power-law index is  $-1.31 \pm 0.07$ , which suggests a spectral density distribution of  $F_\nu \propto \nu^{-0.31}$ . In contrast, the precursor has a much harder spectrum (possible reasons are further discussed in Section 4). For GRB 230903A, we find a power-law index of  $-1.01^{+0.76}_{-0.06}$ , which would suggest an essentially flat spectral density distribution at low energies. For this burst, the cutoff energy  $E_c$  is poorly constrained ( $88^{+388}_{-5}$ ). For GRB 241030B, there is good agreement at the 1- $\sigma$  level between the optical flux and the extrapolation from high energies. This burst’s power-law index is  $-0.85 \pm 0.2$ , which also would suggest a nearly flat spectral density. This observation likely includes flux from the afterglow; however, we note that the extrapolation from the flux in the two subsequent TESS cadences (reported in GCN 38158; Jayaraman et al. 2024) to the time of the trigger lies above the measured flux, even after correcting for the onboard CRM. Any putative contaminating flux would push the optical observation below the extrapolated high-energy SED. GRB 231106A also exhibits prompt optical flux

that is consistent with the extrapolation from high energies, with a power-law cutoff energy that is better constrained than in GRB 230903A ( $E_c = 81.3^{+66.1}_{-31.0}$  keV), and a similar power-law index to GRB 241030B.

### 3.3. GRBs with underpredicted optical emission

For the remainder of the bursts that have a prompt optical detection, and for some of the non-detections, we find that the optical flux falls significantly below the extrapolation from high energies, as shown in Figure 3. For most bursts, a cutoff power-law fits the data better than the Band function. The only exception is GRB 230307A, for which a Band function gives a  $\chi^2$  value comparable to the one for the cutoff power-law fit (moreover, the low-energy photon index and peak/cutoff energies are consistent within 1- $\sigma$  between the two models).

GRB 210204A had multiple episodes of emission separated by tens of seconds. To evaluate the spectral changes between emission episodes, we performed a time-resolved spectral analysis and found significant



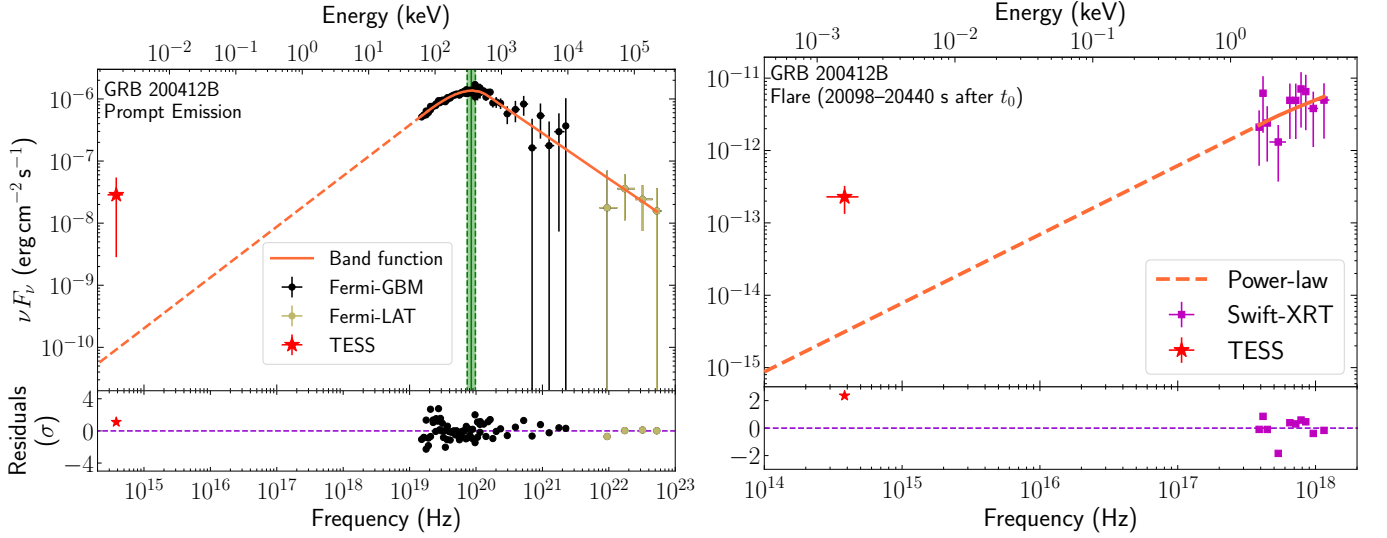


**Figure 1.** Broad-band SEDs for the prompt emission and flare in GRB 200412B. This is the only burst in our sample for which the extrapolation from high energies underpredicts the prompt optical flux (left panel). This underprediction also is observed for the flare occurring at late times (right). The function fit to the data is indicated in the legend. In both cases, the estimated afterglow contribution has been subtracted from the optical flux (red star). The optical flux excess in the prompt emission for GRB 200412B could be explained by an additional component from the reverse shock. The green shading indicates the  $1\text{-}\sigma$  uncertainty region for the power-law turnover for the Band function  $E_p$ . For bursts with Fermi-GBM data, we show spectra from two NaI detectors and one BGO detector. All optical fluxes are corrected for Galactic extinction.

evolution in the power-law index, agreeing with the results from Kumar et al. (2022). However, for both the time-integrated and time-resolved fits, the extrapolation of the high-energy power-law index overpredicts the prompt optical flux. The middle panel of Figure 3 shows the fit to the high-energy emission from the entire duration of the burst, and the fitted parameters agree with those from Kumar et al. (2022).

### 3.4. GRBs with non-detections

Figures 4–6 show the best-fit high-energy SEDs, their extrapolations, and TESS upper limits for the other bursts in our sample, in roughly chronological order. In Figure 6, we show the bursts for which the upper limit on the prompt optical flux lies above the extrapolation from high energies. In these cases, any prompt optical flash not detected by TESS could still be consistent with the extrapolation of the high-energy SED. Table 6 shows the best-fit parameters for the high-energy fit to each of these bursts. For nearly all the long bursts, the prompt optical flux is overpredicted by the extrapolation from high energies. Over half the short and intermediate-duration bursts have limits on optical emission that are overpredicted by the high-energy extrapolation.

Given the presence of prompt Swift-XRT data for GRB 241030A, we compared fits to a Band function to a twice-broken power-law, as postulated by Oganessian et al. (2019). The light curve of GRB 241030A, reported in the GCN of Jayaraman et al. (2024), does not exhibit

any evidence for a prompt flash, and only exhibits a rise and fall typical of afterglows. We fit Swift-XRT, Swift-BAT, Fermi-GBM, and Fermi-LAT data to the `bkn2pow` model in `XSPEC`, as shown in the bottom right panel of Figure 5, and compared this with a fit to the Band function. The Band function, with a break at roughly 100 keV, is strongly favored over the twice-broken power-law for this burst, with a lower  $\chi^2/\text{dof}$ —suggesting that there is no extra spectral break needed to explain our observations. The sharp downturn at low energies seen in the bottom right panel of Figure 5 can likely be attributed to the effects of absorption by intervening hydrogen.

Even if an additional spectral break exists below  $\sim 0.5$  keV, our upper limit on the prompt optical flux is above the extrapolation from high energies, so we cannot confirm or refute such a feature in the SED.

## 4. DISCUSSION

Our results show a clear diversity of relationships between the prompt optical flux from a GRB and the high-energy emission. Only four of the GRBs in our sample of twenty-four have optical fluxes that are consistent with the extrapolation of the high-energy emission to within  $1\text{-}\sigma$ ; the other detections of prompt optical emission differ from the extrapolation from high energies by over  $2\text{-}\sigma$ . In this section, we characterize the nature of the high-energy emission based on our fit parameters and consider possible explanations for the suppressed opti-

Identifier	Type	Fit Interval	Low-energy Photon Index	Cross-Detector Normalization	$E_c$ or $E_p$ (keV)	$\chi^2/\text{dof}$	Flux Limit ( $10^{-12}$ erg $\text{cm}^{-2} \text{s}^{-1}$ )
GRB 180727A	S	$[t_0 - 0.186, t_0 + 1.314]$	$-0.29^{+0.40}_{-0.45}$	$0.83^{+0.12}_{-0.10}$	$40.4^{+19.2}_{-11.0} \star$	122.11/143	0.315
GRB 180924A	L	$[t_0 - 86.13, t_0 + 28.67]$	$-1.95 \pm 0.15$	—	—	61.35/58	0.246
GRB 181022A	I	$[t_0 - 0.71, t_0 + 8.82]$	$-0.87^{+0.48}_{-0.53}$	—	—	48.56/58	0.253
GRB 190422A <sup>‡</sup>	L	$[t_0 + 155, t_0 + 200]$	$-1.51 \pm 0.06$	$1.16^{+0.16}_{-0.13}$	—	339.97/180	0.634
GRB 190630C	L	$[t_0 - 4.69, t_0 + 23.81]$	$-1.88 \pm 0.11$	—	—	65.48/58	0.696
GRB 191016A	L	$[t_0 - 44.17, t_0 + 118.82]$	$-1.65 \pm 0.07$	—	—	40.49/58	0.309
GRB 200303A	L	$[t_0 - 36.88, t_0 + 95.62]$	$-1.35^{+0.10}_{-0.11}$	$0.82^{+0.05}_{-0.04}$	$220.4^{+123.5}_{-63.2} \star$	207.74/204	0.23
GRB 200324A	L*	$[t_0 - 22.51, t_0 + 32.99]$	$-1.57 \pm 0.10$	—	—	44.02/58	0.280
GRB 210419A	L	$[t_0 - 7.9, t_0 + 81.9]$	$-2.13^{+0.32}_{-0.29}$	—	—	52.85/58	$\sim 1$
GRB 210504A	L	$[t_0 - 20, t_0 + 130]$	$-1.57 \pm 0.13$	—	—	59.96/58	0.500
GRB 210730A	I	$[t_0 - 2.17, t_0 + 7.83]$	$-0.93^{+0.17}_{-0.20}$	$0.83^{+0.08}_{-0.07}$	$181.4^{+120.6}_{-63.2} \star$	173.89/175	0.852
GRB 220319A	I	$[t_0 - 1.04, t_0 + 6.96]$	$-2.32^{+0.37}_{-0.32}$	—	—	48.67/58	0.52
GRB 220708A	I	$[t_0 - 3.28, t_0 + 3.36]$	$-2.28^{+0.40}_{-0.33}$	—	—	72.60/58	0.63
GRB 221120A	S	$[t_0 - 0.69, t_0 + 0.37]$	$-0.62^{+0.50}_{-0.23}$	$0.90^{+0.30}_{-0.22}$	$643.6^{+334.6}_{-265.6} \ddagger$	100.42/129	0.892
GRB 230116D	L	$[t_0 - 16.66, t_0 + 75.54]$	$-1.30 \pm 0.29$	—	—	64.64/58	

**Table 6.** Best-fit parameters for power-law fits to GRBs lacking detections of prompt optical emission. Note that the labels for the Type column are as follows: (S) short GRB ( $T_{90} \leq 2$  s); (I) intermediate duration GRB ( $2 < T_{90} < 10$  s); (L) long GRB ( $T_{90} \geq 10$  s). The \* next to GRB 200324A indicates that due to the burst exiting the Swift-BAT field of view between approximately  $t_0 + 100$  s and  $t_0 + 120$  s, a reliable  $T_{90}$  cannot be estimated. We estimate the  $T_{99.5}$  using the available data, but caution that this is affected by the data gap. The <sup>‡</sup> for GRB 190422A indicates that Fermi-GBM data is only available from the second “phase” of the burst, so we analyzed that in conjunction with the same time interval from Swift-BAT (it triggered on the burst  $\gtrsim 150$  s before Fermi-GBM did; the  $t_0$  referenced is from the Swift-BAT data). Cutoff energies from the fits to a cutoff power-law are indicated by a  $\star$ , and peak energies (from fits to a Band function) are indicated by  $\ddagger$ . All  $t_0$  are taken from the Swift-BAT catalog (Lien et al. 2016), even if there was a Fermi-GBM detection.

cal emission relative to the extrapolation of the high energy SED.

#### 4.1. Interpretation of the SEDs

Synchrotron emission in GRBs, which can explain the prompt emission, likely arises from internal shocks in the jet launched by the central engine—typically assumed to be a newly-formed magnetar or a rapidly spinning accreting black hole (e.g., Cenko et al. 2011; Gottlieb et al. 2023). Figure 7 shows that most of the bursts in our sample have spectral indices at energies below the observed break energy ( $E_c$  or  $E_p$ ) consistent with the synchrotron interpretation, although the relationship between the high-energy emission and the prompt optical flash is more varied. It is well-established that the spectral shapes of different emission episodes in a single GRB can vary significantly (e.g., the analyses of the three pulses in GRB 210204A in Section 3 and Kumar et al. 2022, as well as the analysis of GRB 230307A in Dichiara et al. 2023). In fact, for observations of the prompt optical flash that have been obtained at cadences of tens of seconds (as in GRB 050820a; Vestrand et al. 2006), the optical flux can agree with the extrapolation from high energies for certain emission episodes

and not for others. Our time-integrated analysis using TESS makes it difficult to evaluate this hypothesis for the bursts in our sample.

A useful parameter when studying prompt optical emission is the power-law index from the softest high-energy point (typically  $\sim 10$  keV for the majority of bursts in our sample) to the optical flux measurement, referred to as  $\beta_{OX}$ . The distribution of these values is shown in the right panel of Figure 7. There can be significant evolution in the  $\beta_{OX}$  parameter throughout the burst (e.g., Figure 9 of Kopač et al. 2013); TESS’s FFI cadence is too long to resolve such a phenomenon. In our sample, we observe that the majority of bursts with optical detections exhibit a steeper  $\beta_{OX}$  value than the best-fit low-energy gamma-ray slope (i.e., lie above the purple dashed line in Figure 7). In this figure, we also note that the bursts with data only from Swift-BAT appear to be concentrated close to a value of 0 in  $\beta_{OX}$  and power-law indices less than 0.5. This may be a systematic effect, wherein the low-energy power-law index is biased to lower values without higher-energy observations at 100s of keV (e.g., from the Fermi BGO detectors).

Our observation that  $\beta_{OX}$  is typically greater than the low-energy power-law would indicate two possibilities.

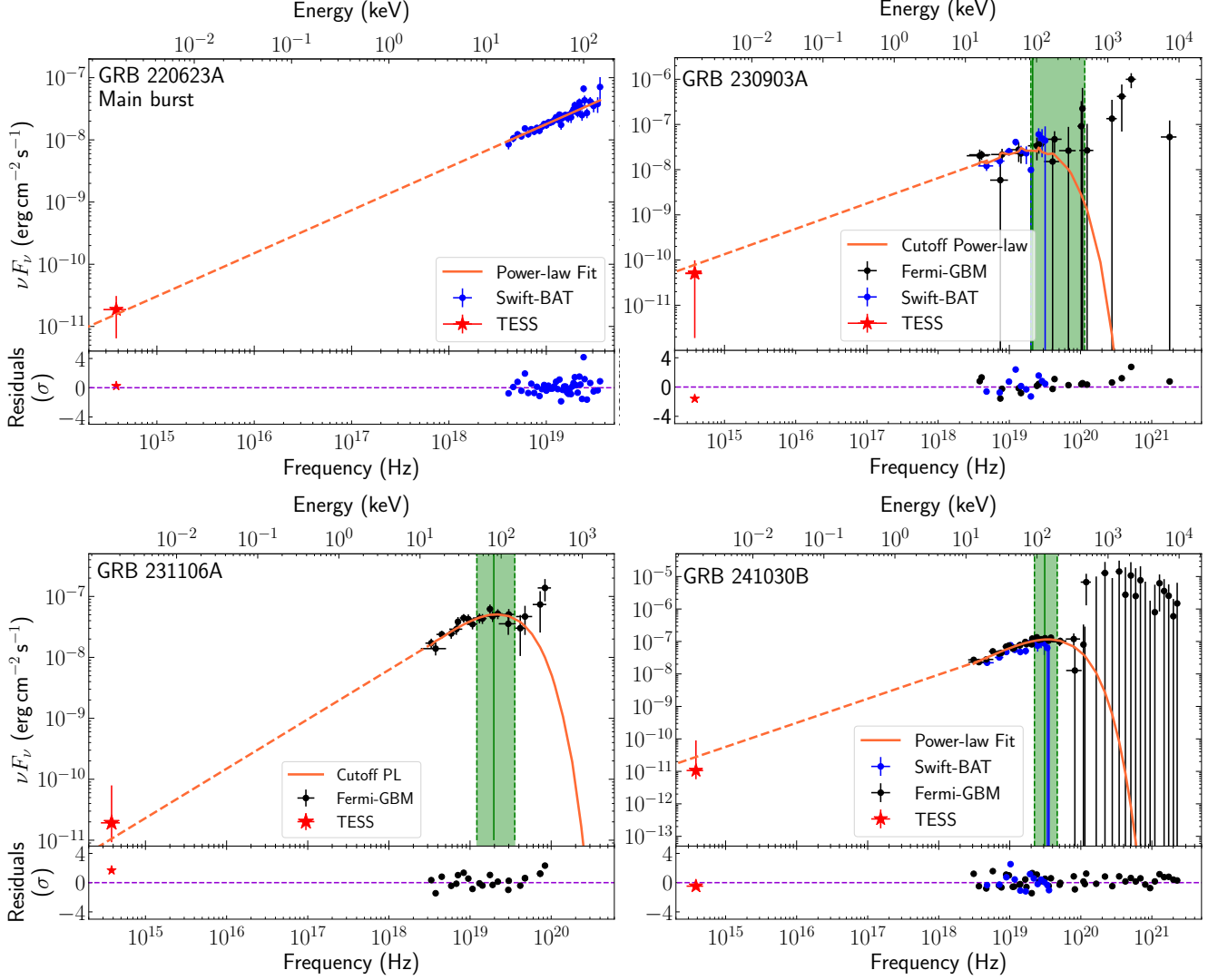


**Figure 2.** As Figure 1, but for bursts where the extrapolation from the high-energy SED is consistent with the estimate for the observed optical flux (at  $1-\sigma$ ). Here, the green shaded region represents the  $1-\sigma$  uncertainty on the cutoff energy for the cutoff power-law model. The BGO data is background-dominated, leading to high uncertainties (e.g., the SED for GRB 241030B).

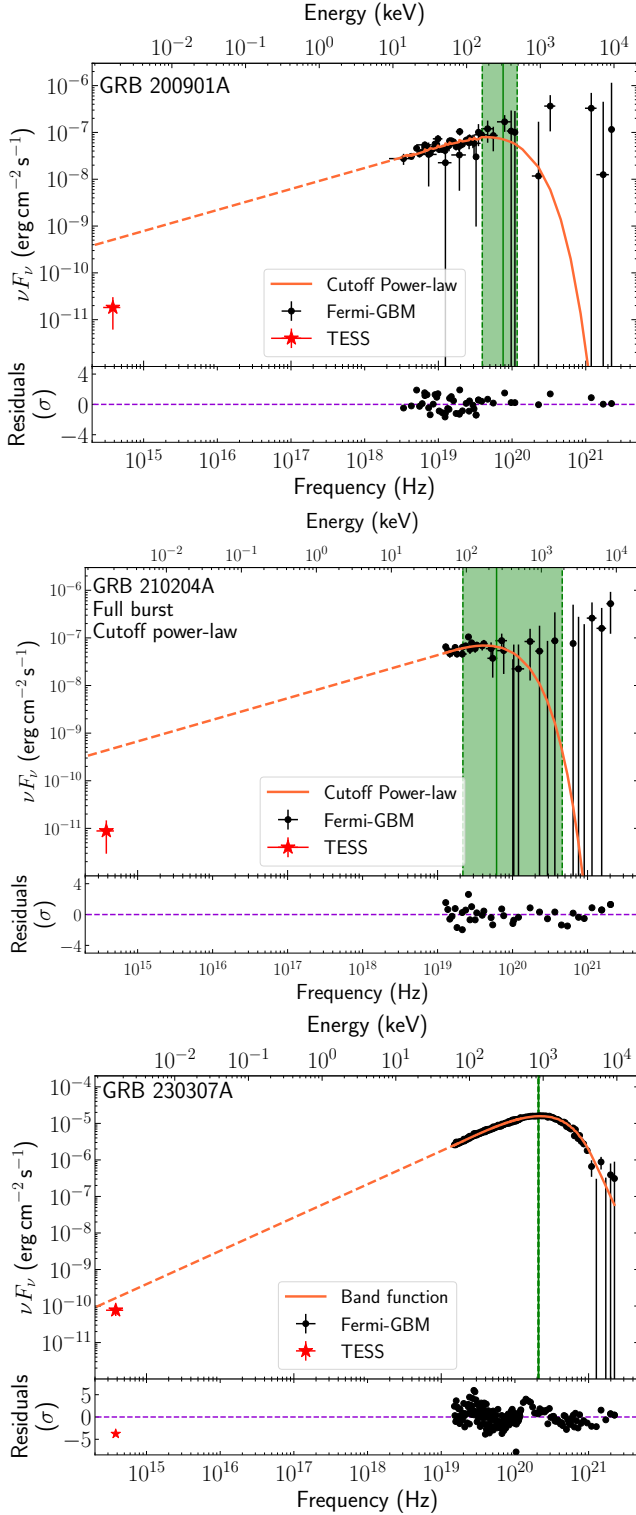


**Figure 3.** As Figures 1-2, but for the three bursts where the extrapolation from high energies overpredicts the prompt optical detection. The deviation of the prompt optical flux from the extrapolation is over  $5\text{-}\sigma$  for GRBs 200901A and 210204A (top and middle panels).

Firstly, there may be a spectral break at low energies that we have not accounted for in our models; secondly, some other phenomenon may suppress the optical emission relative to the extrapolation. We explore various explanations for this observation in Section 4.2.

If synchrotron emission in internal shocks dominates the prompt emission from GRBs, then  $F_\nu \propto \nu^{-0.5}$  (photon index  $-1.5$ ) for the fast cooling regime, i.e., the “low-energy” power-law (Sari et al. 1998; Ghisellini et al. 2000; Uhm & Zhang 2014). The distribution of the power-law index  $\alpha$  is shown in the top panel of Figure 7 (here,  $F_\nu = \nu^\alpha$ ). Theoretically, the maximal value for a power-law index arising from synchrotron emission in a GRB is 0.33 (Preece et al. 1998, also referred to as the “line of death”). Two bursts exhibit harder values of  $\alpha$ , including the short GRB 221120A ( $\alpha = 0.38^{+0.50}_{-0.23}$ ). There are several possible ways to account for these harder values, including incorporating the magnetic field strength in the emission region and/or the presence of thermal or quasi-thermal photospheric emission components (see, e.g., Uhm & Zhang 2014; Ryde 2004; Pe’er et al. 2006).

#### 4.2. Effects of Host Galaxy Extinction

Several bursts from our sample have either optical detections or upper limits that lie below the high-energy extrapolation. Bursts with a high-energy detection but no optical detection (of either prompt or afterglow emission) have been referred to as “dark bursts.” Greiner et al. (2011) suggest three possible causes of an optical non-detection for GRBs: (a) bursts lying at high redshifts, (b) the existence of an intrinsically optically sub-luminous population of GRBs (i.e., with a spectral break in soft X-rays; see Oganessyan et al. 2017), and (c) high line-of-sight extinction. A high line-of-sight extinction could explain the suppression of the optical flux relative to the extrapolation from high energies.

Our sample does not contain any GRBs with confirmed redshifts above  $z \sim 4$  (based on observations reported to the GCN); in fact, the majority of our sample does not have ground-based spectroscopic follow-up that would enable a redshift determination. Consequently, we do not have any way to test the first hypothesis from Greiner et al. Second, given its magnitude limits, TESS would likely be unable to differentiate between an optically sub-luminous GRB population and other extrinsic factors that lead to a non-detection of prompt or afterglow optical emission, such as dust (discussed below) or detector sensitivity. Without ground-based follow-up, we cannot test this hypothesis.

The last possibility from Greiner et al. (2011) is dust extinction. We cannot estimate the extinction without



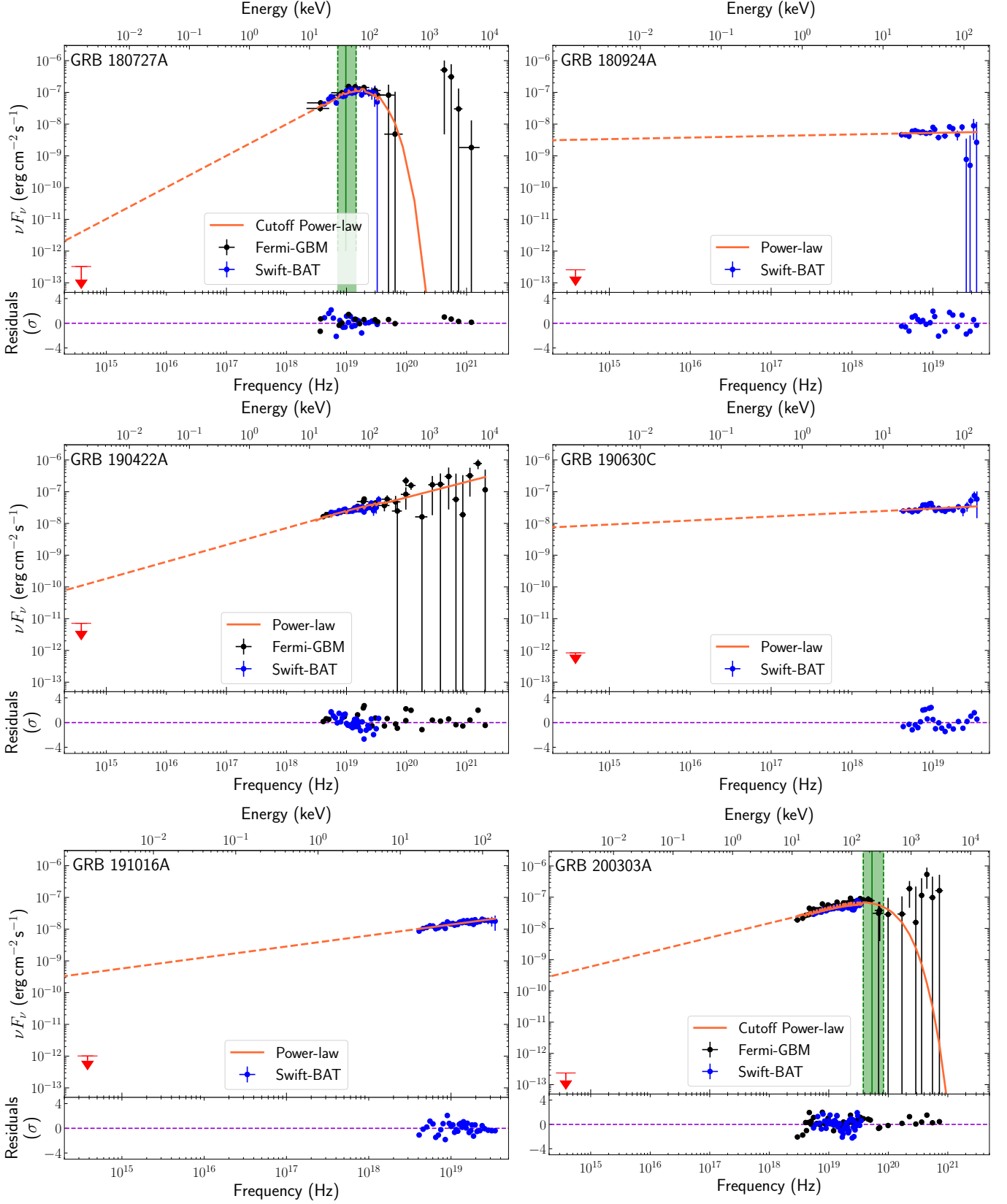


**Figure 4.** As Figures 1–3, but for bursts with upper limits on the prompt optical flux from TESS observations. The bursts in this Figure and Figures 5–6 are displayed in chronological order. We highlight that GRB 180727A is a short burst. These upper limits have been corrected for Galactic extinction.

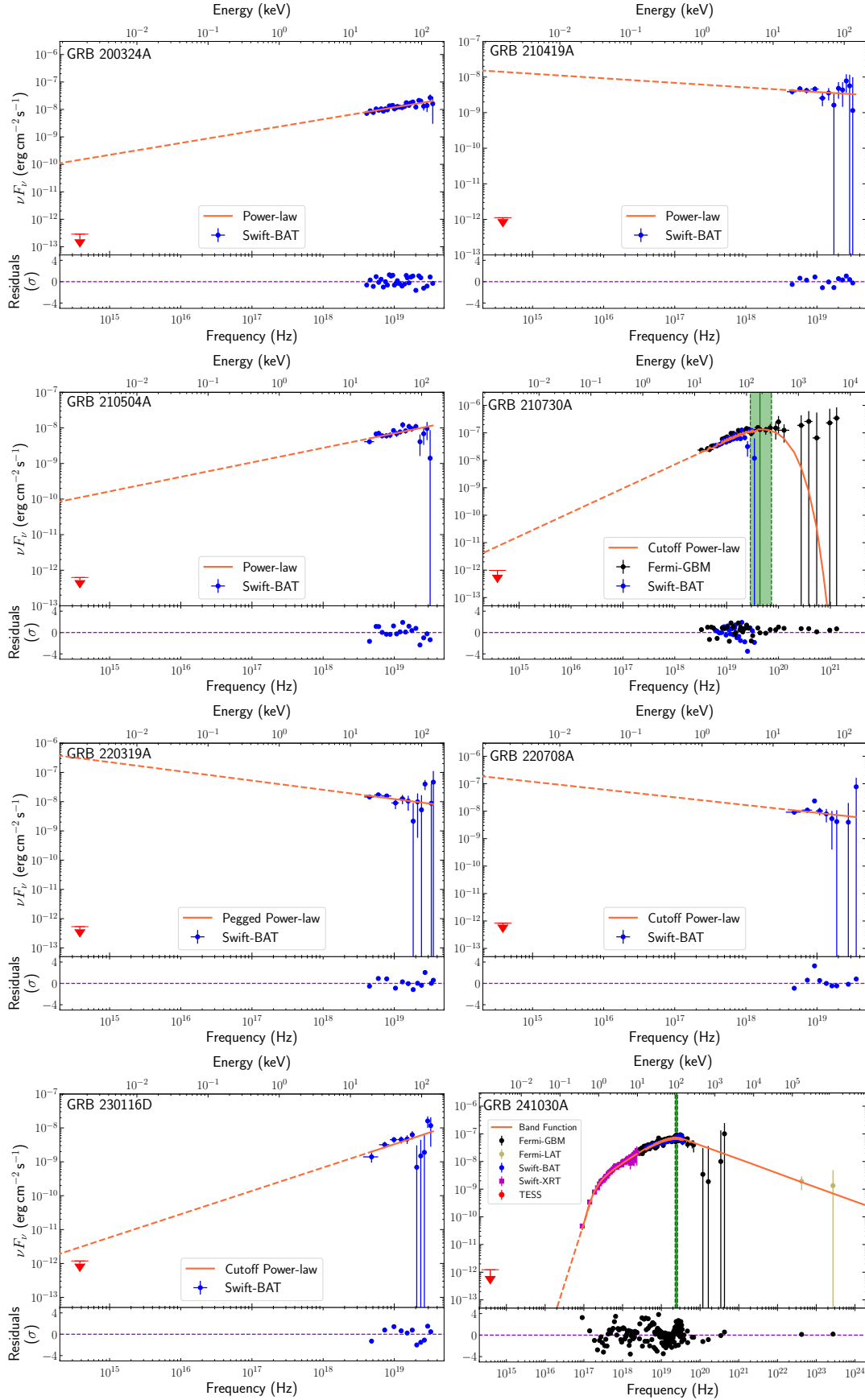


**Figure 5.** Figure 4, continued. All the bursts in this Figure would have had a prompt optical flash that is significantly overpredicted by the extrapolation from the high-energy SED.

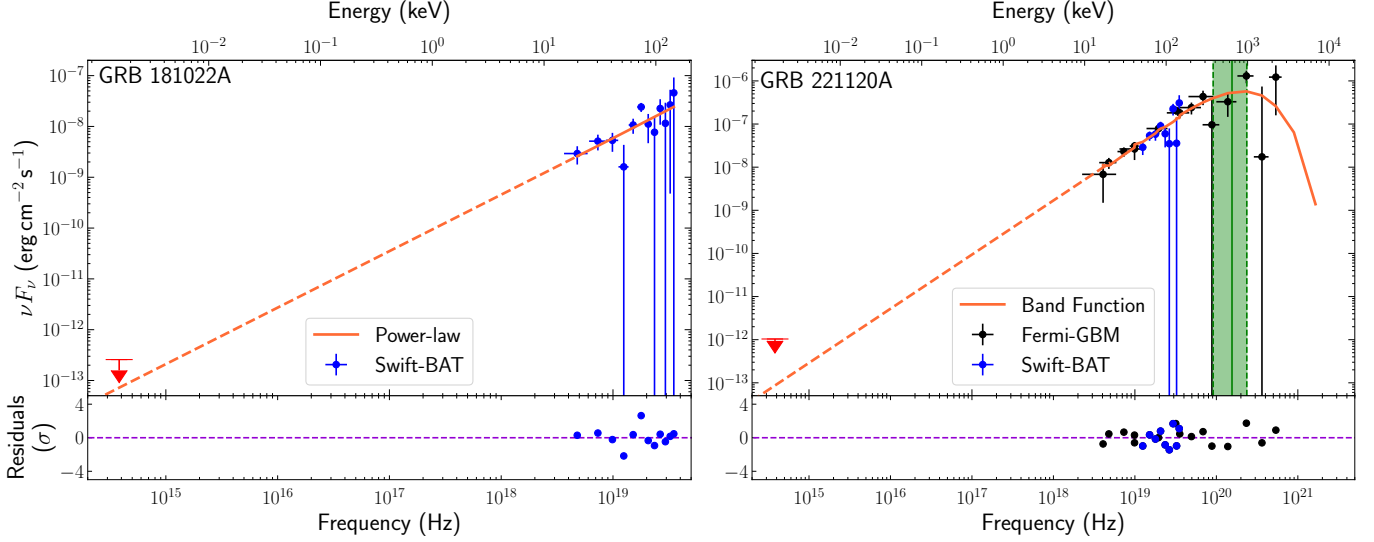


**Figure 6.** As Figures 4–5, but for those bursts for which the upper limit on flux lies above the extrapolation from high energies. We highlight that GRB 221120A is a short burst.

the redshift of the host galaxy, since we require the rest-frame wavelength of the emitted light. However, the extinction is always larger at bluer wavelengths, and so the extinction needed to explain the TESS data in the observed frame (at  $z = 0$ ) is an upper limit on the extinction in the rest frame of the host galaxy. We calculated the extinction required to move the TESS measurements (or upper limits) to the extrapolation of the SED from higher energies, and converted this to an  $A_V$  value using the extinction law from Cardelli et al. (1989), with a standard value  $R_V = 3.1$ . While the LMC extinction law is a better approximation to the extinction law of GRB host galaxies compared to that of Cardelli et al., the two are indistinguishable at  $\lambda \gtrsim 220$  nm (Schady et al. 2012).

The distribution of our calculated  $A_V$  values is shown in Figure 8, alongside an estimate of the hydrogen column density  $N_H$ , assuming  $N_H/A_V \sim 7 \times 10^{21} \text{ cm}^{-2}$ —an approximation to the estimate from Schady et al. (2007). These  $N_H$  values are upper limits, since a smaller column can produce more extinction at bluer optical or UV wavelengths in the host galaxy rest-frame.

We compare our host galaxy  $N_H$  estimates to those provided from the automated fits to Swift-XRT data below 10 keV (Evans et al. 2009) and find that the Swift-XRT fits yield  $A_V \lesssim 1.42$ , which is consistent with our distribution of upper limits in Figure 8. Our derived distribution of the hydrogen column density is consistent with typical galaxy column density sight lines. While this distribution skews to larger values of  $A_V$  than the distributions found by Perley et al. (2009) and Greiner et al. (2011), our values are upper limits (due to the emission in the host galaxy rest-frame being bluer).

There is some agreement between our findings and that from (Perley et al. 2015), in terms of the proportion of GRB host galaxies that have high extinction ( $A_V \gtrsim 6$ ). Further information about a given GRB’s redshift, as well as conclusive host galaxy identifications, will generate more stringent estimates for  $A_V$ .

Oganesyan et al. (2017, 2018, 2019) posit the existence of a spectral break in soft X-rays, which is another possible explanation for these non-detections. However, we could test this hypothesis for only one GRB in our sample (GRB 241030A; bottom right panel of Figure 5); a typical Band function was preferred over a triple broken power-law, disfavoring that hypothesis. For the other bursts, it appears that extinction in the host can explain the suppression/non-detection of optical flux.

#### 4.3. Early Emission and Reverse Shocks in GRBs

When the TESS flux lies considerably above the extrapolation from the high-energy spectrum, as in the cases of GRBs 200412B and 231106A, there may be contributions from other emission components that TESS cannot temporally resolve. The existence of a reverse shock can explain some of the observed excess in the FFI cadence spanning the time of trigger for 200412B.

The reverse shock emission arises from a different region of the GRB than the prompt emission and is not related to internal dissipation processes occurring within the jet itself (see, e.g., the analysis in Oganesyan et al. 2023). Consequently, the TESS detection likely contains multiple emission components. As a result, the prompt emission component is much less than the total flux observed by TESS and may be consistent with the extrapolations from high energies. Moreover, Mészáros & Rees

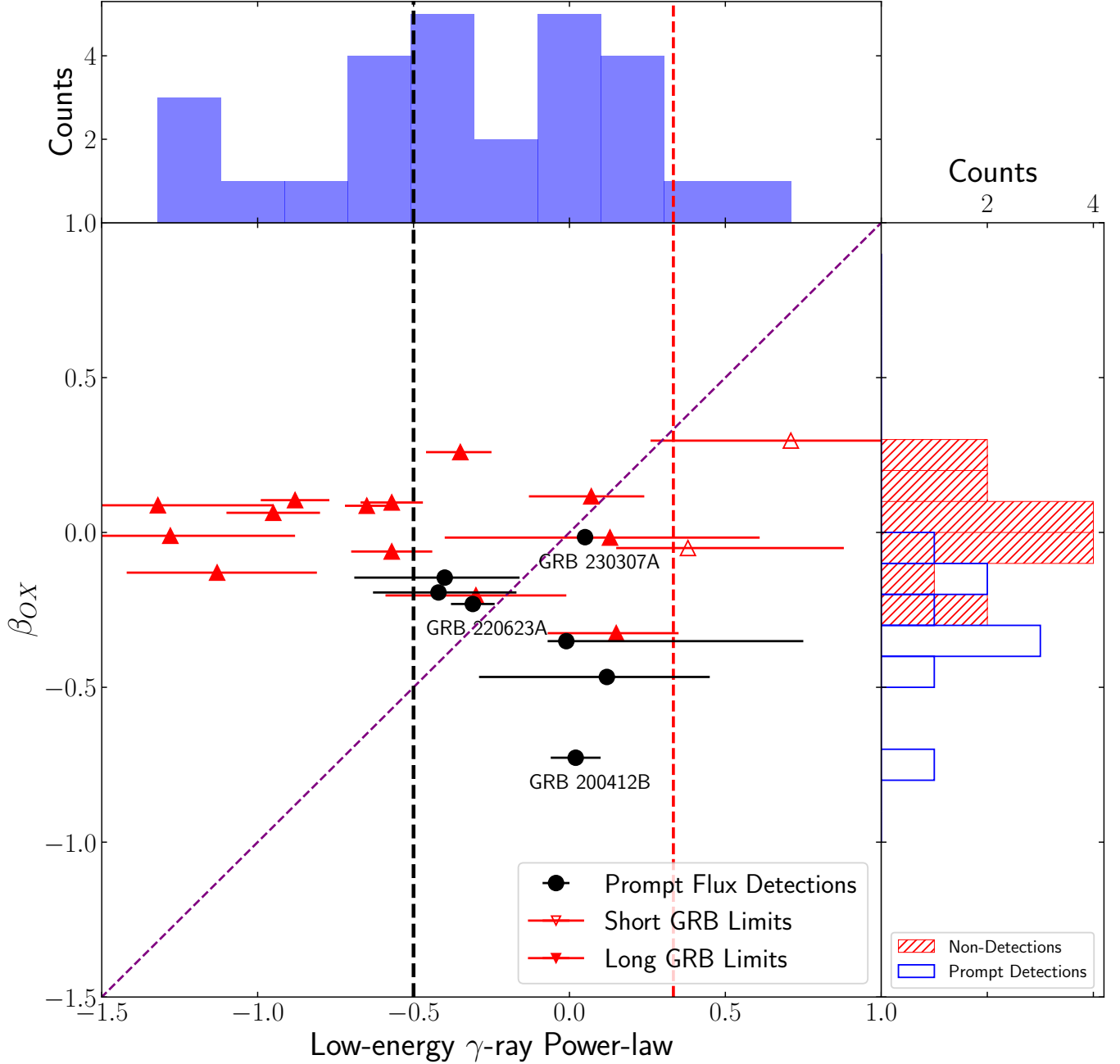


**Figure 7.** The relationship between the gamma-ray to optical spectral slope  $\beta_{OX}$  and the best-fit low-energy gamma-ray spectral index, similar to that shown in Fig. 9 of Kopač et al. (2013). Bursts with detections of prompt optical emission are shown in black, while bursts with upper limits on the prompt optical flux are indicated with red triangles. Long bursts are shown via filled-in triangles; short bursts are not filled in. Three key bursts are annotated on the scatterplot. The line indicating where  $\beta_{OX}$  equals the low-energy power-law index is shown in purple. The synchrotron power-law index for the fast-cooling regime,  $-0.5$ , is shown by the black dashed line, and the low-energy synchrotron limit (Preece et al. 1998) is shown using a red dashed line. Uncertainties are given as 90% confidence intervals. The distribution of power-law indices are plotted alongside the axes. At the top is the distribution of best-fit power-law indices for the high-energy SED (from Tables 4–6); at the right is the distribution of  $\beta_{OX}$ . The distributions for bursts with prompt detections and bursts with upper limits are shown separately, in blue and red, respectively. Note that the more negative the  $\beta_{OX}$ , the higher the likelihood that there is another emission component contributing to the flux observed in the first TESS cadence.



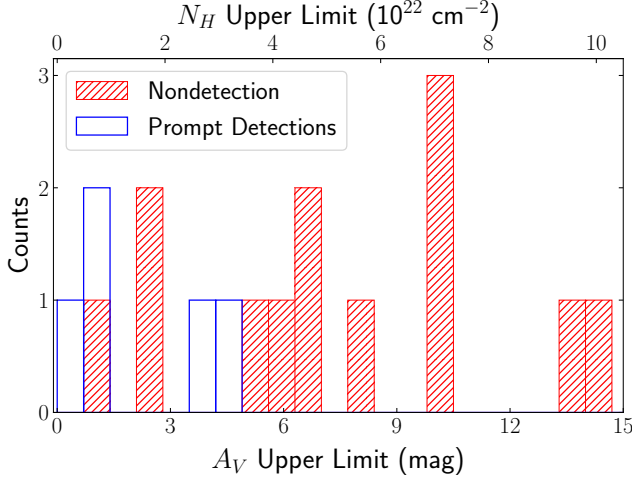


**Figure 8.** The distribution of upper limits on extinction magnitude  $A_V$  based on the suppression of flux relative to the high-energy extrapolation. These values were calculated using the estimate for  $A_{\text{TESS}}$  and a conversion to  $A_V$  using the extinction law of Cardelli et al. (1989), with  $R_V = 3.1$ . We simultaneously show the hydrogen column density values for each bin at the top of the Figure, and use the conversion  $N_H/A_V = 7 \times 10^{21} \text{ cm}^{-2}$  (Schady et al. 2007). Nondetections and detections of prompt optical emission are shown separately, in cross-hatched red and blue, respectively.

(1999) predict that any optical flash from internal shocks should be considerably fainter than the reverse shock emission that would be observed from a GRB. These various arguments suggest that the dominant contributor to the observed TESS flux in GRB 200412B is a reverse shock. Similarly, in GRB 241030A, we observe a change in the light curve slope at  $\sim 2000$  s post-burst, hinting at a transition from reverse to forward shock emission. Other GRBs have reverse shocks peaking tens to hundreds of seconds after the burst (Kobayashi & Zhang 2003; Huang et al. 2016; Oganessian et al. 2023). Radio observations out to  $t_0 + 10$  d can confirm reverse shocks (e.g., Laskar et al. 2013, 2019).

#### 4.4. Caveats for TESS observations of GRBs

While TESS has expanded the sample of GRBs for which prompt optical emission has been detected, its optical measurements are time-integrated over 200 s. This leads to contamination by any additional emission components at optical wavelengths (i.e., either forward or reverse shock emission from the afterglow). In addition, GRBs can show significant spectral evolution on timescales of seconds (e.g., Dichiara et al. 2023), which is averaged over TESS’s 200 s cadence.

An additional factor affecting TESS observations of GRBs the onboard cosmic-ray mitigation algorithm, discussed in Section 2.5. While we have attempted to cor-

rect for this, we impose a strong assumption that the optical light curve is correlated with the gamma-ray light curve, introducing a large systematic uncertainty in our estimate for the correct optical flux values.

## 5. CONCLUSION

In this work, we presented broad-band spectral analyses of eight GRBs with detected (or inferred) prompt optical emission that fell within the TESS field of view during the first six and a half years of its mission. We also calculated upper limits and modeled the prompt emission for 16 other bursts that lacked optical detections in TESS, in order to ascertain why prompt optical flashes are only observed from a subset of bursts.

From our sample:

- We found that one burst exhibited an optical flux excess relative to the extrapolation of the power law from high energies, which we attribute to potential reverse shock emission.
- Four bursts had an optical flux consistent with the extrapolated power-law.
- Nearly all the remaining bursts had prompt optical emission (or upper limits) that was overpredicted by the extrapolation from high energies.
- One of the bursts exhibited a flare roughly  $2 \times 10^4$  s after the trigger that we attribute to late-time central engine activity.

We found that for most bursts, a power-law (or its variants, including a cutoff power-law) or the Band function (Band et al. 1993) fit the high-energy emission well. For the flare in GRB 200412B, while we have only limited data from Swift-XRT, we find that a simple power-law is the best fit to the available data, and that the optical flux is underpredicted by the extrapolation from high energies.

We evaluated several possibilities for the potential non-detections and suppression of the optical flux. The suppression of optical flux relative to the high energy extrapolation can be explained with dust extinction in the host galaxies of these GRBs, as opposed to an extra spectral break at soft X-rays (Oganessian et al. 2017, 2018, 2019). For the one burst for which we were able to test this spectral break hypothesis using prompt Swift-XRT data (GRB 241030A), we found that a regular Band function fit the spectrum better than a twice-broken power-law.

GRB prompt emission is a diverse phenomenon that does not necessarily have a clear-cut explanation—as further observations of GRBs often raise more questions

about the nature of the optical flash. Continued observations by TESS during upcoming its Extended Mission 3, in conjunction with Swift-XRT data and other ground-based follow-up, can help constrain the typical levels of dust extinction in GRB host galaxies. Identification of host galaxies, in addition to redshift estimates for GRBs detected by TESS, would be exceptionally valuable in characterizing bursts for which TESS has detected prompt emission. Finally, a deep search for counterparts to Fermi-GBM-detected bursts in TESS may also illuminate the existence of different classes of GRBs exhibiting prompt optical flashes.

### ACKNOWLEDGMENTS

The authors would like to thank Gor Oganessian for information about synchrotron models. RJ would also like to thank Mike Moss and Brad Cenko for discussions about emission models for GRBs, as well as Mason Ng, Joheen Chakraborty, and Megan Masterson for assistance with XSPEC.

This paper includes data collected by the TESS mission. Funding for the TESS mission is provided by the NASA Explorer Program. The TICA data utilized

in this work was obtained from the MAST archive at [10.17909/t9-9j8c-7d30](https://doi.org/10.17909/t9-9j8c-7d30), hosted by the Space Telescope Science Institute (STScI). STScI is operated by the Association of Universities for Research in Astronomy, Inc., under NASA contract NAS 5–26555.

This work has made use of data supplied by the UK Swift Science Data Centre at the University of Leicester. This research also made use of both Swift and Fermi data provided by the High Energy Astrophysics Science Archive Research Center (HEASARC), a service of the Astrophysics Science Division at NASA/GSFC. Finally, this work also made use of the extinction calculator provided by the NASA/IPAC Extragalactic Database (NED; [10.26132/NED5](https://doi.org/10.26132/NED5)), which is funded by the National Aeronautics and Space Administration and operated by the California Institute of Technology.

*Facilities:* TESS, Swift, Fermi

*Software:* `astropy` (Astropy Collaboration et al. 2013, 2018, 2022), `matplotlib` (Hunter 2007), `numpy` (Harris et al. 2020), `scipy` (Virtanen et al. 2020), Fermi ScienceTools (Fermi Science Support Development Team 2019), XSPEC (Arnaud 1996), `swift-too` (<https://www.swift.psu.edu/tooapi/>), `synphot` (STScI Development Team 2018)

### REFERENCES

- Ajello, M., Arimoto, M., Axelsson, M., et al. 2019, *ApJ*, 878, 52, doi: [10.3847/1538-4357/ab1d4e](https://doi.org/10.3847/1538-4357/ab1d4e)
- Akerlof, C., Balsano, R., Barthelmy, S., et al. 1999, *Nature*, 398, 400, doi: [10.1038/18837](https://doi.org/10.1038/18837)
- Amati, L. 2006, *MNRAS*, 372, 233, doi: [10.1111/j.1365-2966.2006.10840.x](https://doi.org/10.1111/j.1365-2966.2006.10840.x)
- Arnaud, K. A. 1996, in *Astronomical Society of the Pacific Conference Series*, Vol. 101, *Astronomical Data Analysis Software and Systems V*, ed. G. H. Jacoby & J. Barnes, 17
- Astropy Collaboration, Robitaille, T. P., Tollerud, E. J., et al. 2013, *A&A*, 558, A33, doi: [10.1051/0004-6361/201322068](https://doi.org/10.1051/0004-6361/201322068)
- Astropy Collaboration, Price-Whelan, A. M., Sipőcz, B. M., et al. 2018, *AJ*, 156, 123, doi: [10.3847/1538-3881/aabc4f](https://doi.org/10.3847/1538-3881/aabc4f)
- Astropy Collaboration, Price-Whelan, A. M., Lim, P. L., et al. 2022, *ApJ*, 935, 167, doi: [10.3847/1538-4357/ac7c74](https://doi.org/10.3847/1538-4357/ac7c74)
- Atwood, W. B., Abdo, A. A., Ackermann, M., et al. 2009, *ApJ*, 697, 1071, doi: [10.1088/0004-637X/697/2/1071](https://doi.org/10.1088/0004-637X/697/2/1071)
- Band, D., Mateson, J., Ford, L., et al. 1993, *ApJ*, 413, 281, doi: [10.1086/172995](https://doi.org/10.1086/172995)
- Barthelmy, S. D., Cummings, J. R., Gropp, J. D., et al. 2019, *GRB Coordinates Network*, 26012, 1
- Barthelmy, S. D., D’Elia, Krimm, H. A., et al. 2022, *GRB Coordinates Network*, 32361, 1
- Beardmore, A. P., Evans, P. A., Goad, M. R., Osborne, J. P., & Swift-XRT Team. 2024, *GRB Coordinates Network*, 37962, 1
- Beniamini, P., & Piran, T. 2013, *ApJ*, 769, 69, doi: [10.1088/0004-637X/769/1/69](https://doi.org/10.1088/0004-637X/769/1/69)
- Bissaldi, E., & Fermi GBM Team. 2021, *GRB Coordinates Network*, 29393, 1
- Blake, C., & Bloom, J. S. 2004, *ApJ*, 606, 1019, doi: [10.1086/383134](https://doi.org/10.1086/383134)
- Burns, E., Goldstein, A., Lesage, S., Dalessi, S., & Fermi-GBM Team. 2023, *GRB Coordinates Network*, 33414, 1
- Cardelli, J. A., Clayton, G. C., & Mathis, J. S. 1989, *ApJ*, 345, 245, doi: [10.1086/167900](https://doi.org/10.1086/167900)
- Cash, W. 1979, *ApJ*, 228, 939, doi: [10.1086/156922](https://doi.org/10.1086/156922)
- Cenko, S. B., Frail, D. A., Harrison, F. A., et al. 2011, *ApJ*, 732, 29, doi: [10.1088/0004-637X/732/1/29](https://doi.org/10.1088/0004-637X/732/1/29)
- Cheung, C. C., Kerr, M., Grove, J. E., et al. 2023, *GRB Coordinates Network*, 35013, 1
- Dalessi, S., & Fermi GBM Team. 2023, *GRB Coordinates Network*, 33551, 1

- de Barra, C., Meegan, C., & Fermi Gamma-ray Burst Monitor Team. 2024, GRB Coordinates Network, 38015, 1
- Dichiara, S., Tsang, D., Troja, E., et al. 2023, *ApJL*, 954, L29, doi: [10.3847/2041-8213/acf21d](https://doi.org/10.3847/2041-8213/acf21d)
- Evans, P. A., Goad, M. R., Osborne, J. P., Beardmore, A. P., & Swift-XRT Team. 2024, GRB Coordinates Network, 37992, 1
- Evans, P. A., Beardmore, A. P., Page, K. L., et al. 2009, *MNRAS*, 397, 1177, doi: [10.1111/j.1365-2966.2009.14913.x](https://doi.org/10.1111/j.1365-2966.2009.14913.x)
- Fan, Y.-Z., Zhang, B., & Wei, D.-M. 2009, *PhRvD*, 79, 021301, doi: [10.1103/PhysRevD.79.021301](https://doi.org/10.1103/PhysRevD.79.021301)
- Fausnaugh, M. M., Burke, C. J., Ricker, G. R., & Vanderspek, R. 2020, *Research Notes of the American Astronomical Society*, 4, 251, doi: [10.3847/2515-5172/abd63a](https://doi.org/10.3847/2515-5172/abd63a)
- Fausnaugh, M. M., Valley, P. J., Kochanek, C. S., et al. 2021, *ApJ*, 908, 51, doi: [10.3847/1538-4357/abcd42](https://doi.org/10.3847/1538-4357/abcd42)
- Fausnaugh, M. M., Valley, P. J., Tucker, M. A., et al. 2023a, *arXiv e-prints*, arXiv:2307.11815, doi: [10.48550/arXiv.2307.11815](https://doi.org/10.48550/arXiv.2307.11815)
- Fausnaugh, M. M., Jayaraman, R., Vanderspek, R., et al. 2023b, *Research Notes of the American Astronomical Society*, 7, 56, doi: [10.3847/2515-5172/acc4c5](https://doi.org/10.3847/2515-5172/acc4c5)
- Fermi Science Support Development Team. 2019, *Fermitools: Fermi Science Tools, Astrophysics Source Code Library*, record ascl:1905.011
- Gehrels, N., Chincarini, G., Giommi, P., et al. 2004, *ApJ*, 611, 1005, doi: [10.1086/422091](https://doi.org/10.1086/422091)
- Ghisellini, G., Celotti, A., & Lazzati, D. 2000, *MNRAS*, 313, L1, doi: [10.1046/j.1365-8711.2000.03354.x](https://doi.org/10.1046/j.1365-8711.2000.03354.x)
- Gottlieb, O., Metzger, B. D., Quataert, E., et al. 2023, *ApJL*, 958, L33, doi: [10.3847/2041-8213/ad096e](https://doi.org/10.3847/2041-8213/ad096e)
- Greiner, J., Wenzel, W., Hudec, R., et al. 1995, in *IAU Colloq. 151: Flares and Flashes*, ed. J. Greiner, H. W. Duerbeck, & R. E. Gershberg, Vol. 454, 381, doi: [10.1007/3-540-60057-4\\_314](https://doi.org/10.1007/3-540-60057-4_314)
- Greiner, J., Krühler, T., Klose, S., et al. 2011, *A&A*, 526, A30, doi: [10.1051/0004-6361/201015458](https://doi.org/10.1051/0004-6361/201015458)
- Grove, J. E., Cheung, C. C., Kerr, M., et al. 2020, in *Gamma-ray Bursts in the Gravitational Wave Era 2019*, ed. T. Sakamoto, M. Serino, & S. Sugita, 57–59, doi: [10.48550/arXiv.2009.11959](https://doi.org/10.48550/arXiv.2009.11959)
- Gruber, D., Goldstein, A., Weller von Ahlefeld, V., et al. 2014, *ApJS*, 211, 12, doi: [10.1088/0067-0049/211/1/12](https://doi.org/10.1088/0067-0049/211/1/12)
- Guiriec, S., Gonzalez, M. M., Sacahui, J. R., et al. 2016a, *ApJ*, 819, 79, doi: [10.3847/0004-637X/819/1/79](https://doi.org/10.3847/0004-637X/819/1/79)
- Guiriec, S., Mochkovitch, R., Piran, T., et al. 2015a, *ApJ*, 814, 10, doi: [10.1088/0004-637X/814/1/10](https://doi.org/10.1088/0004-637X/814/1/10)
- Guiriec, S., Kouveliotou, C., Daigne, F., et al. 2015b, *ApJ*, 807, 148, doi: [10.1088/0004-637X/807/2/148](https://doi.org/10.1088/0004-637X/807/2/148)
- Guiriec, S., Kouveliotou, C., Hartmann, D. H., et al. 2016b, *ApJL*, 831, L8, doi: [10.3847/2041-8205/831/1/L8](https://doi.org/10.3847/2041-8205/831/1/L8)
- Hamburg, R., Fletcher, C., & Meegan, C. 2019, GRB Coordinates Network, 24161, 1
- Harris, C. R., Millman, K. J., van der Walt, S. J., et al. 2020, *Nature*, 585, 357, doi: [10.1038/s41586-020-2649-2](https://doi.org/10.1038/s41586-020-2649-2)
- HI4PI Collaboration, Ben Bekhti, N., Flöer, L., et al. 2016, *A&A*, 594, A116, doi: [10.1051/0004-6361/201629178](https://doi.org/10.1051/0004-6361/201629178)
- Horack, J. M. 1991, *Development of the Burst And Transient Source Experiment (BATSE)*.
- Huang, X.-L., Xin, L.-P., Yi, S.-X., et al. 2016, *ApJ*, 833, 100, doi: [10.3847/1538-4357/833/1/100](https://doi.org/10.3847/1538-4357/833/1/100)
- Hunter, J. D. 2007, *Computing in Science and Engineering*, 9, 90, doi: [10.1109/MCSE.2007.55](https://doi.org/10.1109/MCSE.2007.55)
- Jayaraman, R., Fausnaugh, M., & Ricker, G. R. 2024, GRB Coordinates Network, 38158, 1
- Jayaraman, R., Fausnaugh, M., Ricker, G. R., Vanderspek, R., & Mo, G. 2024, *ApJ*, 972, 162, doi: [10.3847/1538-4357/ad5e7b](https://doi.org/10.3847/1538-4357/ad5e7b)
- Jayaraman, R., Fausnaugh, M., Vanderspek, R., & Ricker, G. R. 2024, GRB Coordinates Network, 38134, 1
- Jayaraman, R., Fausnaugh, M. M., Vanderspek, R., & Ricker, G. R. 2023a, GRB Coordinates Network, 34650, 1
- Jayaraman, R., Vanderspek, R., Fausnaugh, M. M., Mo, G., & Ricker, G. R. 2023b, GRB Coordinates Network, 35047, 1
- Kaastra, J. S., & Bleeker, J. A. M. 2016, *A&A*, 587, A151, doi: [10.1051/0004-6361/201527395](https://doi.org/10.1051/0004-6361/201527395)
- Klotz, A., Boër, M., Atteia, J. L., & Gendre, B. 2009, *AJ*, 137, 4100, doi: [10.1088/0004-6256/137/5/4100](https://doi.org/10.1088/0004-6256/137/5/4100)
- Klotz, A., Gendre, B., Stratta, G., et al. 2006, *A&A*, 451, L39, doi: [10.1051/0004-6361:20065158](https://doi.org/10.1051/0004-6361:20065158)
- Kobayashi, S., & Zhang, B. 2003, *ApJL*, 582, L75, doi: [10.1086/367691](https://doi.org/10.1086/367691)
- Kopač, D., Kobayashi, S., Gomboc, A., et al. 2013, *ApJ*, 772, 73, doi: [10.1088/0004-637X/772/1/73](https://doi.org/10.1088/0004-637X/772/1/73)
- Krimm, H. A., Vanderspek, R. K., & Ricker, G. R. 1996, *A&AS*, 120, 251
- Krimm, H. A., Barthelmy, S. D., Cummings, J. R., et al. 2019, GRB Coordinates Network, 24941, 1
- Krimm, H. A., Barthelmy, S. D., Laha, S., et al. 2022, GRB Coordinates Network, 31781, 1
- Kumar, H., Gupta, R., Saraogi, D., et al. 2022, *MNRAS*, 513, 2777, doi: [10.1093/mnras/stac1061](https://doi.org/10.1093/mnras/stac1061)
- Kumar, P., & McMahon, E. 2008, *MNRAS*, 384, 33, doi: [10.1111/j.1365-2966.2007.12621.x](https://doi.org/10.1111/j.1365-2966.2007.12621.x)
- Laha, S., Barthelmy, S. D., Beardmore, A. P., et al. 2021, GRB Coordinates Network, 29939, 1

- Laha, S., Barthelmy, S. D., Gupta, R., et al. 2024, GRB Coordinates Network, 38011, 1
- Laskar, T., Berger, E., Zauderer, B. A., et al. 2013, ApJ, 776, 119, doi: [10.1088/0004-637X/776/2/119](https://doi.org/10.1088/0004-637X/776/2/119)
- Laskar, T., van Eerten, H., Schady, P., et al. 2019, ApJ, 884, 121, doi: [10.3847/1538-4357/ab40ce](https://doi.org/10.3847/1538-4357/ab40ce)
- Li, R. Z., Lin, H., Li, S. S., et al. 2024, GRB Coordinates Network, 38027, 1
- Li, Z., & Waxman, E. 2008, ApJL, 674, L65, doi: [10.1086/529042](https://doi.org/10.1086/529042)
- Lien, A., Sakamoto, T., Barthelmy, S. D., et al. 2016, ApJ, 829, 7, doi: [10.3847/0004-637X/829/1/7](https://doi.org/10.3847/0004-637X/829/1/7)
- Lien, A. Y., Barthelmy, S. D., Beardmore, A. P., et al. 2018, GRB Coordinates Network, 23047, 1
- Longo, F., Kocsievski, D., Bissaldi, E., et al. 2020, GRB Coordinates Network, 27557, 1
- Mailyan, B., Hamburg, R., & Fermi GBM Team. 2020, GRB Coordinates Network, 27558, 1
- Malacaria, C., Meegan, C., & Fermi GBM Team. 2020, GRB Coordinates Network, 27314, 1
- Markwardt, C. B., Barthelmy, S. D., Krimm, H. A., et al. 2023, GRB Coordinates Network, 33194, 1
- Meegan, C., Lichti, G., Bhat, P. N., et al. 2009, ApJ, 702, 791, doi: [10.1088/0004-637X/702/1/791](https://doi.org/10.1088/0004-637X/702/1/791)
- Mészáros, P., & Rees, M. J. 1999, MNRAS, 306, L39, doi: [10.1046/j.1365-8711.1999.02800.x](https://doi.org/10.1046/j.1365-8711.1999.02800.x)
- Moss, M. J., Barthelmy, S. D., D’Ai, A., et al. 2023, GRB Coordinates Network, 34623, 1
- Narayana Bhat, P., Meegan, C. A., von Kienlin, A., et al. 2016, ApJS, 223, 28, doi: [10.3847/0067-0049/223/2/28](https://doi.org/10.3847/0067-0049/223/2/28)
- Oganesyan, G., Nava, L., Ghirlanda, G., & Celotti, A. 2017, ApJ, 846, 137, doi: [10.3847/1538-4357/aa831e](https://doi.org/10.3847/1538-4357/aa831e)
- . 2018, A&A, 616, A138, doi: [10.1051/0004-6361/201732172](https://doi.org/10.1051/0004-6361/201732172)
- Oganesyan, G., Nava, L., Ghirlanda, G., Melandri, A., & Celotti, A. 2019, A&A, 628, A59, doi: [10.1051/0004-6361/201935766](https://doi.org/10.1051/0004-6361/201935766)
- Oganesyan, G., Karpov, S., Salafia, O. S., et al. 2023, Nature Astronomy, 7, 843, doi: [10.1038/s41550-023-01972-4](https://doi.org/10.1038/s41550-023-01972-4)
- Palmer, D. M., Barthelmy, S. D., Cenko, S. B., et al. 2020, GRB Coordinates Network, 27311, 1
- Palmer, D. M., Barthelmy, S. D., Cummings, J. R., et al. 2021, GRB Coordinates Network, 29838, 1
- Parsotan, T., Barthelmy, S. D., Krimm, H. A., et al. 2022, GRB Coordinates Network, 32264, 1
- Pe’er, A., Mészáros, P., & Rees, M. J. 2006, ApJ, 642, 995, doi: [10.1086/501424](https://doi.org/10.1086/501424)
- Pereyra, M., Fraija, N., Watson, A. M., et al. 2022, MNRAS, 511, 6205, doi: [10.1093/mnras/stac389](https://doi.org/10.1093/mnras/stac389)
- Perley, D. A., Cenko, S. B., Bloom, J. S., et al. 2009, AJ, 138, 1690, doi: [10.1088/0004-6256/138/6/1690](https://doi.org/10.1088/0004-6256/138/6/1690)
- Perley, D. A., Perley, R. A., Hjorth, J., et al. 2015, ApJ, 801, 102, doi: [10.1088/0004-637X/801/2/102](https://doi.org/10.1088/0004-637X/801/2/102)
- Pillera, R., Gupta, R., Kocevski, D., Loizzo, P., & Fermi-LAT Collaboration. 2024, GRB Coordinates Network, 37979, 1
- Preece, R. D., Briggs, M. S., Mallozzi, R. S., et al. 1998, ApJL, 506, L23, doi: [10.1086/311644](https://doi.org/10.1086/311644)
- Racusin, J. L., Karpov, S. V., Sokolowski, M., et al. 2008, Nature, 455, 183, doi: [10.1038/nature07270](https://doi.org/10.1038/nature07270)
- Ricker, G. R., Winn, J. N., Vanderspek, R., et al. 2015, Journal of Astronomical Telescopes, Instruments, and Systems, 1, 014003, doi: [10.1117/1.JATIS.1.1.014003](https://doi.org/10.1117/1.JATIS.1.1.014003)
- Ryde, F. 2004, ApJ, 614, 827, doi: [10.1086/423782](https://doi.org/10.1086/423782)
- Sakamoto, T., Lamb, D. Q., Kawai, N., et al. 2005, ApJ, 629, 311, doi: [10.1086/431235](https://doi.org/10.1086/431235)
- Sakamoto, T., Hullinger, D., Sato, G., et al. 2008, ApJ, 679, 570, doi: [10.1086/586884](https://doi.org/10.1086/586884)
- Sakamoto, T., Barthelmy, S. D., Cummings, J. R., et al. 2019, GRB Coordinates Network, 24157, 1
- . 2020, GRB Coordinates Network, 28344, 1
- Sakamoto, T., Barthelmy, S. D., Krimm, H. A., et al. 2021, GRB Coordinates Network, 30554, 1
- . 2022, GRB Coordinates Network, 32970, 1
- Sari, R., & Piran, T. 1997, MNRAS, 287, 110, doi: [10.1093/mnras/287.1.110](https://doi.org/10.1093/mnras/287.1.110)
- . 1999, ApJ, 520, 641, doi: [10.1086/307508](https://doi.org/10.1086/307508)
- Sari, R., Piran, T., & Narayan, R. 1998, ApJL, 497, L17, doi: [10.1086/311269](https://doi.org/10.1086/311269)
- Schady, P., Mason, K. O., Page, M. J., et al. 2007, MNRAS, 377, 273, doi: [10.1111/j.1365-2966.2007.11592.x](https://doi.org/10.1111/j.1365-2966.2007.11592.x)
- Schady, P., Dwelly, T., Page, M. J., et al. 2012, A&A, 537, A15, doi: [10.1051/0004-6361/201117414](https://doi.org/10.1051/0004-6361/201117414)
- Schlafly, E. F., & Finkbeiner, D. P. 2011, ApJ, 737, 103, doi: [10.1088/0004-637X/737/2/103](https://doi.org/10.1088/0004-637X/737/2/103)
- Shrestha, M., Steele, I. A., Kobayashi, S., et al. 2022, MNRAS, 509, 5964, doi: [10.1093/mnras/stab3368](https://doi.org/10.1093/mnras/stab3368)
- Smith, K. L., Ridden-Harper, R., Fausnaugh, M., et al. 2021, ApJ, 911, 43, doi: [10.3847/1538-4357/abe6a2](https://doi.org/10.3847/1538-4357/abe6a2)
- Stamatikos, M., Barthelmy, S. D., Cummings, J. R., et al. 2018a, GRB Coordinates Network, 23264, 1
- . 2018b, GRB Coordinates Network, 23365, 1
- STScI Development Team. 2018, synphot: Synthetic photometry using Astropy, Astrophysics Source Code Library, record ascl:1811.001. <http://ascl.net/1811.001>
- Swenson, C. A., Roming, P. W. A., De Pasquale, M., & Oates, S. R. 2013, ApJ, 774, 2, doi: [10.1088/0004-637X/774/1/2](https://doi.org/10.1088/0004-637X/774/1/2)



- Troja, E., Lipunov, V. M., Mundell, C. G., et al. 2017, *Nature*, 547, 425, doi: [10.1038/nature23289](https://doi.org/10.1038/nature23289)
- Uhm, Z. L., & Zhang, B. 2014, *Nature Physics*, 10, 351, doi: [10.1038/nphys2932](https://doi.org/10.1038/nphys2932)
- Ukwatta, T. N., Barthelmy, S. D., Cummings, J. R., et al. 2020, *GRB Coordinates Network*, 27443, 1
- Vanderspek, R., Fausnaugh, M. M., Jayaraman, R., et al. 2023, *GRB Coordinates Network*, 33453, 1
- Veres, P. 2018, *GRB Coordinates Network*, 23044, 1
- Veres, P., Hamburg, R., Meegan, C., & Fermi GBM Team. 2020, *GRB Coordinates Network*, 28340, 1
- Veres, P., Meegan, C., & Fermi GBM Team. 2022, *GRB Coordinates Network*, 32964, 1
- Vestrand, W. T., Woźniak, P. R., Wren, J. A., et al. 2005, *Nature*, 435, 178, doi: [10.1038/nature03515](https://doi.org/10.1038/nature03515)
- Vestrand, W. T., Wren, J. A., Woźniak, P. R., et al. 2006, *Nature*, 442, 172, doi: [10.1038/nature04913](https://doi.org/10.1038/nature04913)
- Vestrand, W. T., Wren, J. A., Panaitescu, A., et al. 2014, *Science*, 343, 38, doi: [10.1126/science.1242316](https://doi.org/10.1126/science.1242316)
- Virtanen, P., Gommers, R., Oliphant, T. E., et al. 2020, *Nature Methods*, 17, 261, doi: [10.1038/s41592-019-0686-2](https://doi.org/10.1038/s41592-019-0686-2)
- von Kienlin, A., Meegan, C. A., Paciesas, W. S., et al. 2014, *ApJS*, 211, 13, doi: [10.1088/0067-0049/211/1/13](https://doi.org/10.1088/0067-0049/211/1/13)
- . 2020, *ApJ*, 893, 46, doi: [10.3847/1538-4357/ab7a18](https://doi.org/10.3847/1538-4357/ab7a18)
- Wei, J., Cordier, B., Antier, S., et al. 2016, *arXiv e-prints*, arXiv:1610.06892, doi: [10.48550/arXiv.1610.06892](https://doi.org/10.48550/arXiv.1610.06892)
- Williams, G. G., Milne, P. A., Park, H. S., et al. 2008, in *American Institute of Physics Conference Series*, Vol. 1000, *Gamma-ray Bursts 2007*, ed. M. Galassi, D. Palmer, & E. Fenimore, 535–538, doi: [10.1063/1.2943525](https://doi.org/10.1063/1.2943525)
- Wilms, J., Allen, A., & McCray, R. 2000, *ApJ*, 542, 914, doi: [10.1086/317016](https://doi.org/10.1086/317016)
- Wood, J., & Fermi GBM Team. 2021, *GRB Coordinates Network*, 30557, 1
- Xin, L., Han, X., Li, H., et al. 2023, *Nature Astronomy*, 7, 724, doi: [10.1038/s41550-023-01930-0](https://doi.org/10.1038/s41550-023-01930-0)
- Yuan, W., Zhang, C., Chen, Y., & Ling, Z. 2022, in *Handbook of X-ray and Gamma-ray Astrophysics*, 86, doi: [10.1007/978-981-16-4544-0\\_151-1](https://doi.org/10.1007/978-981-16-4544-0_151-1)
- Yuan, W., Zhang, C., Ling, Z., et al. 2018, in *Society of Photo-Optical Instrumentation Engineers (SPIE) Conference Series*, Vol. 10699, *Space Telescopes and Instrumentation 2018: Ultraviolet to Gamma Ray*, ed. J.-W. A. den Herder, S. Nikzad, & K. Nakazawa, 1069925, doi: [10.1117/12.2313358](https://doi.org/10.1117/12.2313358)
- Zheng, W., Brink, T. G., Filippenko, A. V., Yang, Y., & KAIT GRB Team. 2024, *GRB Coordinates Network*, 37959, 1

## APPENDIX

## A. BURST-SPECIFIC ANALYSIS

Best-fit spectra and the optical fluxes (or limits on these fluxes) are shown in Figures 1–3 and 4–6, respectively. Bursts are discussed in chronological order in this section. Best-fit parameters for fits to the spectra of these bursts are given in Tables 4–6. Constraints on the hydrogen column density and dust extinction in these GRBs’ host galaxies are shown in Figure 8. Here, we give detailed notes on individual GRBs. As a reminder, the power-law indices that we report are photon spectrum indices. In this section, we report negative power-law indices for both the Band fits and the (cutoff) power-law fits, in the interest of consistency. Note that our convention for the power-law differs from that of XSPEC, which reports positive exponents for power laws.

## A.1. Bursts with Prompt Detections

*GRB 200412B*—This GRB peaked between 13–14th magnitude (using the estimate from J24) and exhibited an optical flare approximately 0.25 d post-burst. This GRB was also detected at high energies by Fermi-LAT (Longo et al. 2020), with 11 photons detected between  $t_0$  and  $t_0 + 20$  s. This data allows for more stringent constraints on the power-law index at high energies ( $\beta$ ) for the Band function. The data from TESS, Fermi-GBM, and Fermi-LAT, along with the best fit model, are shown in Figure 1. While fitting, we masked out data less than 60 keV, due to the Iodine K-edge (30–50 keV) causing systematic issues.

A Band function (shown in the top left panel of Figure 1) yielded a much better fit to the data than a cutoff power-law. We compared our values to the initial analysis from the GCN of Mailyan et al. (2020). Their peak energy ( $E_p = 257 \pm 4$  keV) agrees with ours to within  $2\sigma$ ; however, Mailyan et al. report  $\alpha = -0.54 \pm 0.01$  and  $\beta = -2.24 \pm 0.02$ , which differ by over  $5\sigma$  from our values of  $\alpha = -0.98 \pm 0.08$  and  $\beta = -2.73 \pm 0.09$ . We attribute the difference in the high-energy slope  $\beta$  to the inclusion of Fermi-LAT data in our fit, while Mailyan et al. fit only Fermi-GBM data between 50–300 keV.

The cutoff power-law model significantly underpredicts the flux in the Fermi-LAT regime, due to the exponential decrease in the model flux. Experimenting with the addition of a blackbody to the cutoff power-law, as in Oganessian et al. (2017, 2018, 2019), does not improve the fit. Both the Band model and the cutoff power-law model disagree with the TESS flux when extrapolated to those lower frequencies. The excess TESS flux above the high-energy extrapolation suggests the presence of an additional emission component, such as a reverse shock. Further interpretation of these results can be found in Section 4.

We additionally note that Longo et al. reported a 1.1 GeV photon arrival at  $t_0 + 134$  s, in addition to the 11 photons that were detected by the LAT during the prompt emission phase of the burst. However, this highly energetic photon is unlikely to be related to the GRB prompt emission based on its timing. If we add only the promptly-detected Fermi-LAT photons to the flux calculation, we obtain a value of  $7.77 \times 10^{-6} \text{ erg cm}^{-2} \text{ s}^{-1}$  for the gamma-ray flux, and  $2.00 \times 10^{-4} \text{ erg cm}^{-2}$  for the gamma-ray fluence.

*GRB 200901A*—This GRB had a  $3.8\sigma$  detection in TESS of prompt emission at the time of the trigger. This burst was detected by both Swift-BAT and Fermi-GBM, so we used both data sets for the fit. We found that a cutoff power-law (shown in the top panel of Figure 3) was able to model the combination of the two data sets, accounting for a constant multiplicative offset. The power-law index is consistent with that found by both Sakamoto et al. (2020) ( $\alpha = -1.72 \pm 0.11$ ) and Veres et al. (2020) ( $\alpha = -1.52 \pm 0.09$ ); Veres et al. also find a cutoff energy of  $E_c = 410 \pm 150$  keV, which agrees with our best-fit value  $E_c = 313_{-150}^{+173}$ . Our model has a flux in the 10 – 1000 keV range of  $6.47 \times 10^{-7} \text{ erg cm}^{-2} \text{ s}^{-1}$ ; over the interval we consider, the fluence is  $1.64 \times 10^{-5} \text{ erg cm}^{-2}$ .

We find that an extrapolation of this power law significantly overpredicts the optical flux, by over an order of magnitude. The GRB trigger occurred roughly 140 s before the end of the corresponding FFI cadence in TESS. As a result, we must evaluate the possibility whether this detection, and the (fainter) detection in the next cadence, are early detections of the afterglow. The TESS data for the transient suggests that it is fading, meaning that the afterglow peak must be between the time of trigger  $t_0$  and the end of the corresponding FFI,  $t_0 + 140$  s. This information can be utilized to constrain the bulk Lorentz factor of the burst  $\Gamma_0$ . To do so, we can use a photometric redshift estimate from Legacy Survey imaging, as there is a galaxy located 1” from this GRB with  $\text{photo-}z = 1.209 \pm 0.329$  ( $D_L \sim 8.4$  Gpc).

We find an isotropic GRB energy  $E_{\text{iso}}$  of approximately  $10^{52}$  erg, modulo a small  $k$ -correction factor (of order unity).<sup>14</sup> Thus, we estimate  $\Gamma_0$  to be approximately 200, up to a factor of  $(\eta_{0.2}n_0)^{-1/8}$  (typically roughly of order unity), which accounts for the dependence on the circum-burst density  $n_0$  and the radiative efficiency  $\eta$  normalized to 0.2. Some of the emission observed in the cadence contemporaneous with the trigger could arise from the afterglow, although there are only two TESS data points above the detection limit for this burst. Given that these results are in line with typical parameters for GRBs derived from analyses of their afterglows, we cannot conclusively state that the entirety of the detection in this cadence is from a prompt optical counterpart.

If what was observed is afterglow emission, then there still would exist a significant discrepancy between an upper limit on the prompt emission, and the extrapolation of the high-energy spectrum.

*GRB 210204A*—This GRB had three distinct emission episodes, with four peaks during a single 600 s TESS cadence. We analyzed each of the three emission episodes independently, as well as in a time-averaged manner, to study the spectral evolution of the burst.

First, we analyzed the full burst emission. We fit both a Band function and a cutoff power-law to the data, and found that a cutoff power-law is slightly preferred (based on the  $\chi^2/\text{dof}$  reported in Tables 4 and 5), with an index of  $-1.30^{+0.51}_{-0.81}$ . This index agrees with that from Kumar et al. (2022). Our cutoff energy is slightly higher (albeit considerably more uncertain) than the  $E_p$  values reported by both Kumar et al. or the GCN of Bissaldi & Fermi GBM Team (2021), who report  $E_p = 140 \pm 50$  keV. The total flux from the burst over the 10–1000 keV range was  $3.45 \times 10^{-7} \text{ erg cm}^{-2} \text{ s}^{-1}$ ; this yields a total gamma-ray fluence of  $1.36 \times 10^{-4} \text{ erg cm}^{-2}$ . At the redshift of  $z = 0.876$  from Kumar et al., which corresponds to a luminosity distance of  $D_L \approx 5.7$  Gpc, we find  $E_{\text{iso}} \sim 2.8 \times 10^{53}$ , which is of a similar order of magnitude as the total energy calculated from summing all three episodes'  $E_{\text{iso}}$  in Kumar et al.

To test whether the optical emission could have arisen from the brightest portion of the burst (the third emission episode), we also performed a spectral fit to this time range. A Band function was slightly preferred for this portion of the burst; 90% confidence intervals for our parameters are given in Table 4. The flux for this portion of the burst was  $8.79 \times 10^{-7} \text{ erg cm}^{-2} \text{ s}^{-1}$ ; the fluence was  $1.12 \times 10^{-4} \text{ erg cm}^{-2}$ , making the estimate of  $E_{\text{iso}}$  during this portion of the burst roughly  $2.3 \times 10^{53}$  erg. Our power-law index for the third episode ( $-1.4 \pm 0.3$ ) is in good agreement with that from Kumar et al.:  $-1.30 \pm 0.04$ . Discrepancies between our analyses could arise from the fact that we used a much longer time range than they did; they selected just the  $T_{90}$  (for the entire burst and also for each peak), while we selected a longer portion of the burst emission ( $T_{99.5}$ ). Spectral evolution throughout the intervals that they did not consider could also play a role in our larger error bars.

*GRB 220623A*—This GRB had a  $13\text{-}\sigma$  detection of prompt emission in TESS. In the Swift-BAT light curve, we saw a precursor to the burst spanning from approximately 4 s before the trigger, to 2 s before the trigger. We modeled this precursor's spectrum using a pegged power-law, as described above, and found a power-law index of  $0.70 \pm 0.14$ . This precursor lasted 1.5 s, and the flux (between 15–150 keV) is  $2.4 \times 10^{-7} \text{ erg cm}^{-2} \text{ s}^{-1}$ , with a fluence of  $3.6 \times 10^{-7} \text{ erg cm}^{-2}$ . Physical explanations for the precursor are further discussed in Section 4.

We then fit a pegged power-law to the main burst (from  $t_0$  to  $t_0 + 53$  s (shown in the top left panel of Figure 2) and found a power-law index of  $-1.31 \pm 0.07$ , which agrees with the value from Parsotan et al. (2022),  $\alpha = 1.33 \pm 0.07$ . Extrapolation of the full burst spectrum shows that the optical flux detected in TESS is consistent with this power-law. The main burst had a flux of  $5.03 \times 10^{-8} \text{ erg cm}^{-2} \text{ s}^{-1}$ , and an overall fluence of  $3.21 \times 10^{-6} \text{ erg cm}^{-2}$ . Note that due to TESS's temporal resolution, we were unable to determine whether the optical flux arose from the precursor, or during the main burst emission itself.

We note an anomalous feature in the Swift-BAT spectrum near around 90 keV, which could be related to an absorption edge from lead at 88 keV—a detector systematic discussed at [https://swift.gsfc.nasa.gov/analysis/bat\\_digest.html](https://swift.gsfc.nasa.gov/analysis/bat_digest.html).

*GRB 230307A*—This GRB is the first one for which TESS has observed both a prompt emission component and an afterglow (Vanderspek et al. 2023; Fausnaugh et al. 2023b; Jayaraman et al. 2024). Broad-band spectral modeling for this source is complicated by the fact that different portions of the burst's prompt emission have different spectral properties (Dichiara et al. 2023). Our analysis of this source used time-integrated data, as the TESS data does not have the temporal resolution required to differentiate between the various emission periods described in Dichiara et al. This may increase the uncertainties in the Band function parameters, as they significantly evolve throughout the burst.

<sup>14</sup> While the cutoff energy  $E_c$  is poorly constrained, it still seems consistent with the Amati relation (Amati 2006).

We found that a Band function (shown in the bottom panel of Figure 3) was the best fit to the data, with a well-constrained low-energy power-law slope of  $-0.95 \pm 0.01$  and a peak energy  $E_p \sim 865$  keV. We also masked out all the data below 50 keV for this burst due to the anomalous detector response of the NaI detectors at these energies. The flux of our model, between 10–1000 keV, is  $5.1 \times 10^{-5}$  erg cm $^{-2}$  s $^{-1}$ ; over the range of our data, we calculate a fluence of  $5.2 \times 10^{-3}$  erg cm $^{-2}$ . The extrapolation of the power-law to the TESS frequency overpredicts the observed flux by  $4\text{-}\sigma$ .

Our values for the low-energy power-law, as well as the peak/cutoff energy, are similar to those from Burns et al. (2023) but are formally discrepant at  $5\text{-}\sigma$  (they find a power-law index of  $-1.07 \pm 0.01$  and a cutoff energy of  $936 \pm 3$  keV. This could be attributed to our decision to include the “bad time intervals” reported by Dalessi & Fermi GBM Team (2023), as the data are usable (priv. comm., C. M. Hui).

*GRB 230903A*—This GRB was an intermediate-duration burst, with a  $T_{90}$  of approximately 2.5 s. It was also an X-ray rich burst, as defined in Sakamoto et al. (2008), wherein the ratio of the fluence from 25–50 keV to that from 50–100 keV is between 0.72 and 1.32. There was a  $5\text{-}\sigma$  detection of prompt emission in TESS at the time of trigger (GCN 34650, Jayaraman et al. 2023a; and J24).

The best-fitting model for this burst was a cutoff power-law; we used data from both Swift-BAT and Fermi-GBM for our fit. Our power-law index of  $-1.01^{+0.76}_{-0.06}$  is consistent with that reported by Moss et al. (2023),  $\alpha = 1.40 \pm 0.21$ . The TESS flux is consistent at the  $1\text{-}\sigma$  level with the extrapolation of the burst power-law to low frequencies (as seen in the top right panel of Figure 2). For this burst, we find a flux (in the 10–1000 keV band) of  $1.61 \times 10^{-7}$  erg cm $^{-2}$  s $^{-1}$ , and a fluence of  $8.2 \times 10^{-7}$  erg cm $^{-2}$ .

*GRB 231106A*—This burst was the first poorly-localized burst with an arcsecond-localized counterpart in TESS data, as reported by GCN 35047 (Jayaraman et al. 2023b). It had a  $T_{90}$  of approximately 60 seconds, and exhibited a flux excess in the TESS FFI cadence spanning the trigger time. The burst occurred 107.96 s before the end of that FFI cadence; the entirety of the emission was contained within one FFI, and there is no evidence of a precursor in the Fermi-GBM light curve. We corrected the measured flux for the extrapolated afterglow contribution, which was presumed to start at  $t_0 + 60$  s, and applied the CRM correction as described in J24. This yielded an extinction-corrected prompt optical flux of roughly  $3.15 \times 10^{-11}$  erg cm $^{-2}$  s $^{-1}$ , measured over a  $T_{90}$  of approximately 60 s.

We use the Fermi-GBM data to constrain the low-energy spectral index using a cutoff power-law (shown in the bottom left panel of Figure 2). This model in line with that used by Cheung et al. (2023) to analyze data for this GRB from the Glowbug satellite (Grove et al. 2020). A cutoff power-law is strongly preferred over a single power-law due to the downturn at higher energies, and it is very slightly preferred over a Band function. The index from Glowbug is  $-2.0$ , while our power-law index is  $-0.88^{+0.33}_{-0.41}$ —differing by roughly  $3\text{-}\sigma$ .

We find that the extrapolation of this burst’s spectrum into the optical is consistent with the TESS observation; both the high-energy spectrum and the TESS flux are shown in the bottom left panel of Figure 2. The total flux (from 10–1000 keV) is  $1.63 \times 10^{-7}$  erg cm $^{-2}$  s $^{-1}$ , and the total fluence is  $\sim 10^{-5}$  erg cm $^{-2}$ . However, because there is no clear host galaxy, we do not have a redshift estimate with which to calculate  $E_{\text{iso},\gamma}$  for this burst.

*GRB 241030B*—This burst was observed by both Swift-BAT and Fermi-GBM. TESS observed a decaying optical transient over hundreds of seconds. This light curve likely had contributions from both a prompt optical flash, as well as a decaying afterglow. If we assume that the entirety of the emission observed in the initial cadence was from the prompt optical flash, the CRM correction yields a magnitude of 15.84, with the brightest 20 s flash having a magnitude of 13.16. If we assume that the entirety of the prompt optical flash occurred during the  $T_{99.5}$  (10.4 s), we find a magnitude of 12.64. However, we note that if there is a contribution from the afterglow in the cadence corresponding to the high-energy trigger, this would make the estimated magnitudes fainter.

We fit both the Swift-BAT and Fermi-GBM data to a cutoff power-law and found an index of  $-0.85 \pm 0.20$ —a  $2\text{-}\sigma$  discrepancy with Laha et al. (2024) ( $-1.4 \pm 0.16$ ). This discrepancy may likely arise from our inclusion of the Fermi-GBM data, as Laha et al. only used Swift-BAT data. Both data sets, as well as the TESS upper limit, are shown in the bottom right of Figure 2. The TESS detection is consistent with the extrapolation from high energies.

## A.2. Bursts with Upper Limits

*GRB 180727A*—This short burst was detected by both Fermi-GBM and Swift-BAT; however, the data from the Fermi-GBM BGO detector was background-dominated, with  $> 99\%$  of the counts arising from background activity. A joint fit to the Swift-BAT and two Fermi-GBM NaI detectors showed that a cutoff power law fit was slightly preferred over



a Band model fit. Our power-law index and cutoff energy of  $-0.29 \pm 0.4$  and  $40.4 \pm 20$  roughly agree with the best-fit values from Veres (2018,  $\alpha = -0.14 \pm 0.28$ ,  $E_c = 69 \pm 4$ ) and Lien et al. (2018,  $\alpha = -0.59 \pm 0.51$ ,  $E_p = 67.6 \pm 14.8$ ). The optical upper limit lies below the  $1\text{-}\sigma$  extrapolation of the power-law (top left of Figure 4).

*GRB 180924A*—We fit a pegged power-law to the Swift-BAT data and found a strong disagreement between the extrapolation of this power-law and the optical flux limit by three orders of magnitude. Our best-fit power-law index of  $-1.95 \pm 0.15$  agrees with Stamatikos et al. (2018a), who report  $\alpha = -1.94 \pm 0.14$ . The best-fit power-law and TESS limit are shown in the top right of Figure 4.

*GRB 181022A*—We fit a pegged power-law to the Swift-BAT data and found a highly uncertain power-law index, with a fractional uncertainty of over 50%. Our best-fit power law index of  $-0.87^{+0.48}_{-0.53}$  is consistent with that of Stamatikos et al. (2018b,  $-0.78 \pm 0.41$ ). The limit from TESS lies above the extrapolation. The best-fit power-law is shown in the left panel of Figure 6.

*GRB 190422A*—This burst exhibited two distinct phases of emission; Swift-BAT observed both phases, while Fermi-GBM only observed the second. As a result, we fit only the data from the second phase of emission, from roughly 155–200 s post-burst, to ensure more accurate constraints on the power-law parameters by using multiple data sets. For this burst, a simple power-law was preferred over a cutoff power law or a Band function. The optical upper limit for this burst is two orders of magnitude below the power-law extrapolation. The power-law index that we obtained,  $-1.51 \pm 0.06$ , is consistent with those reported by Hamburg et al. (2019,  $-1.57 \pm 0.14$ ) and Sakamoto et al. (2019,  $-1.76 \pm 0.08$ ) at the  $2\text{-}\sigma$  level; however, these GCNs reported analyses based only on the earlier phase of the burst. The best-fit power-law and TESS limit are shown in the middle left panel of Figure 4.

*GRB 190630C*—We fit a pegged power-law to this burst, and found a very well-constrained power-law index. The index that we find,  $-1.88 \pm 0.11$  agrees with that reported by Krimm et al. (2019,  $-1.96 \pm 0.11$ ). The discrepancy between the high-energy flux and the optical upper limit is over four orders of magnitude. Both the power-law and the TESS limit are shown in the middle right panel of Figure 4.

*GRB 191016A*—The TESS light curve was published in Smith et al. (2021), and exhibits a rising and falling afterglow over  $\sim 10^4$  s, without any evidence for prompt emission. We fit a pegged power-law to this burst’s Swift-BAT data and found a value for the power-law index ( $-1.65 \pm 0.07$ ) consistent with that reported in the GCN of Barthelmy et al. (2019,  $-1.55 \pm 0.09$ ). The TESS limit on the prompt flux from this burst is roughly 3 orders of magnitude below the extrapolation. Both the power-law and the TESS flux limit are shown in the bottom left panel of Figure 4. Analyses of this burst and the high-energy emission can also be found in Shrestha et al. (2022) and Pereyra et al. (2022).

*GRB 200303A*—This GRB had data from both Fermi-GBM and Swift-BAT. We jointly fit a cutoff power law to both data sets, and found a low-energy power law index ( $-1.35 \pm 0.11$ ) that is consistent with the results from both Swift-BAT (Palmer et al. 2020,  $-1.39 \pm 0.17$ ) and Fermi-GBM (Malacaria et al. 2020,  $-1.26 \pm 0.05$ ). The optical upper limit deviates by over three orders of magnitude from the power-law extrapolation; both of these are shown in the bottom right panel of Figure 4.

*GRB 200324A*—We fit a pegged power-law to the Swift-BAT data and found a value for the power-law index ( $-1.57 \pm 0.10$ ) consistent with the value reported in Ukwatta et al. (2020,  $-1.72 \pm 0.15$ ). We note that this burst was out of the BAT FOV for 20 seconds; any burst emission during this phase would not have been part of our spectral analysis, and the true power-law index may differ. After extrapolating to optical wavelengths, we find that the optical upper limit is over two orders of magnitude lower than the extrapolated power-law. Both the power-law and the optical upper limit are shown in the top left panel of Figure 5.

*GRB 210419A*—We fit a pegged power-law to the Swift-BAT data for this burst. Our obtained power-law index ( $-2.13 \pm 0.30$ ) is in good agreement with that from Palmer et al. (2021,  $-2.17 \pm 0.24$ ). The extrapolation to the optical disagrees with the optical flux limit by four orders of magnitude. The best-fit power-law and the optical flux limit from TESS are shown in the top right panel of Figure 5.

*GRB 210504A*—We fit a pegged power-law to the Swift-BAT data for this burst. Our obtained power-law index ( $-1.57 \pm 0.13$ ) is in good agreement with that from Laha et al. (2021,  $-1.64 \pm 0.1$ ). The extrapolation to the optical disagrees with the optical flux limit by over two orders of magnitude. The best-fit power-law and the optical flux limit

from TESS are shown in the second from top, left panel of Figure 5. This burst had an afterglow detected in TESS (J24), but did not exhibit any evidence for a prompt optical flash.

*GRB 210730A*—This GRB had data from both Fermi-GBM and Swift-BAT, which we used to perform a joint fit. A cutoff power-law fit the joint data set better than a Band function. The power-law index that we calculate for this burst ( $-0.93 \pm 0.20$ ) is consistent with that from Wood & Fermi GBM Team (2021,  $-0.68 \pm 0.07$ ) to within their mutual  $1\text{-}\sigma$  uncertainties, as is the cutoff energy ( $\sim 180$ , compared to  $\sim 170$ ). The power-law index deviates more from the estimate in Sakamoto et al. (2021,  $-1.41 \pm 0.11$ ), though it is still statistically consistent with their estimate. The extrapolation to optical wavelengths is roughly the same order of magnitude as the optical upper limit. The best-fit power-law and optical upper limit are shown in the second from top, right panel of Figure 5.

*GRB 220319A*—We fit a pegged power-law to the Swift-BAT data. We find that this burst could belong to the category of X-ray rich bursts (Sakamoto et al. 2005), based on the fluence ratio between low and high energies. The power-law index that we calculate ( $-2.32 \pm 0.35$ ) agrees with that from Krimm et al. (2022,  $-2.15 \pm 0.28$ ). However, the TESS optical flux limit deviates from the power-law extrapolation by over five orders of magnitude, making this the burst with the most discrepant optical flux. This burst’s spectrum, best-fit power-law, and TESS optical upper limit are shown in the third from top, left panel of Figure 5.

*GRB 220708A*—We fit a pegged power-law to the Swift-BAT data and found a power-law ( $-2.28 \pm 0.40$ ) consistent with the value from Barthelmy et al. (2022,  $2.31 \pm 0.32$ ). The extrapolation to the optical disagrees with the flux limit by over five orders of magnitude, similar to the disagreement in GRBs 210419A and 220319A. The best-fit spectrum and TESS upper limit are shown in the third from top, right panel of Figure 6.

*GRB 221120A*—This burst was the first short burst in the TESS field of view after its full-frame image cadence was reduced to 200 s. We used both the Swift-BAT and Fermi-GBM data, and found that a Band function yielded the best fit to the data. The power-law index obtained ( $-0.62^{+0.50}_{-0.23}$ ) is consistent with both the results from Veres et al. (2022,  $-0.11 \pm 0.31$ ) and Sakamoto et al. (2022,  $-0.85 \pm 0.27$ ). The upper limit for the optical flux lies above the power-law extrapolation. Both the best-fit spectrum and the TESS optical upper limit are shown in the right panel of Figure 6.

*GRB 230116D*—We fit a pegged power-law to the Swift-BAT data and found a power-law ( $-1.30 \pm 0.29$ ) consistent with the value from Markwardt et al. (2023,  $-1.38 \pm 0.22$ ). The extrapolation to the optical disagrees with the flux limit by a factor of roughly 3. The best-fit spectrum and TESS upper limit are shown in the bottom left panel of Figure 6. This burst had an afterglow detected in TESS (J24), but did not show any evidence for a prompt optical flash.

*GRB 241030A*—This burst was the brightest burst observed in TESS as part of our sample, with the optical afterglow light curve peaking at a magnitude of  $T \sim 12$  (slightly brighter than 200412B). We used data from Swift-XRT, Swift-BAT, Fermi-GBM, and Fermi-LAT, and fit the observed SED using both a Band function and a twice-broken power-law. We found that a Band function provided a slightly better fit than the twice-broken power-law. Our fit disagrees with that reported by de Barra et al. (2024) by several  $\sigma$ ; this discrepancy likely arises from their use of only the Fermi-GBM data. We find  $\alpha = -1.04 \pm 0.04$ ,  $\beta = -2.51 \pm 0.06$ , and  $E_p = 101 \pm 7$  keV; they find  $\alpha = -1.35 \pm 0.02$ ,  $\beta = -2.31 \pm 0.08$ , and  $E_p = 129 \pm 7$  keV. Our inclusion of both the Fermi-LAT and Swift-XRT data has strongly constrained the low- and high-energy power-law indices, with fractional uncertainties of  $\lesssim 4\%$ . The TESS upper limit lies well above the extrapolation from the Swift-XRT spectrum; the four data sets and the optical upper limit are shown in the bottom right panel of Figure 5.